SANDIA REPORT

SAND2004-5496
Unlimited Release
Printed November 2004

Development of an Efficient Large-Aperture High Damage-Threshold Sol-gel Diffraction Grating

Patrick K. Rambo, Jens Schwarz, Ian C. Smith,
Carol S. Ashley, Eric D. Branson, Darren R. Dunphy, Adam W. Cook,
Scott T. Reed, and William A. Johnson

Prepared by
Sandia National Laboratories
Albuquerque, New Mexico 87185 and Livermore, California 94550

Sandia is a multiprogram laboratory operated by Sandia Corporation,
a Lockheed Martin Company, for the United States Department of Energy's
National Nuclear Security Administration under Contract DE-AC04-94AL85000.

Issued by Sandia National Laboratories, operated for the United States Department of Energy by Sandia Corporation.

Available to DOE and DOE contractors from
U.S. Department of Energy
Office of Scientific and Technical Information
P.O. Box 62
Oak Ridge, TN 37831

Telephone: (865)576-8401
Facsimile: (865)576-5728
E-Mail: reports@adonis.osti.gov
Online ordering: http://www.osti.gov/bridge

Available to the public from
U.S. Department of Commerce
National Technical Information Service
5285 Port Royal Rd
Springfield, VA 22161

Telephone: (800)553-6847
Facsimile: (703)605-6900
E-Mail: orders@ntis.fedworld.gov
Online order: http://www.ntis.gov/help/ordermethods.asp?loc=7-4-0#online

SAND 2004-5496
Unlimited Release
Printed March 2005

Development of an Efficient Large-Aperture High Damage-Threshold Sol-gel Diffraction Grating

Patrick K. Rambo[1], Jens Schwarz[1], Ian C. Smith[1],
Carol S. Ashley[2], Eric D. Branson[2], Darren R. Dunphy[2], Adam W. Cook[2],
Scott T. Reed[3], and
William A. Johnson[4]

Z-Pinch Experiments and Advanced Diagnostics Department[1]
AML Operations[2]
Ceramics and Glass Processing Department[3]
Electromagnetics and Plasma Physics Analysis[4]
Sandia National Laboratories
P.O. Box 5800
Albuquerque, New Mexico 87185-1193

Abstract

In order to develop the next generation of high peak intensity lasers, new grating technology providing higher damage thresholds and large apertures is required. The current assumption is that this technical innovation will be multilayer dielectric gratings, wherein the uppermost layer of a thin film mirror is etched to create the desired binary phase grating. A variant of this is explored with the upper grating layer being a lower density gelatin-based volume phase grating in either sol-gel or dichromated gelatin. One key benefit is the elimination of the etching step.

Intentionally Left Blank

Contents

Figures

Tables

Acknowledgments:

The authors are grateful to our colleagues for the electron micrographs used in this report: Yi Yang, University of New Mexico Research Assistant Professor; Ralf Koehn, visiting scientist, Hamburg, Germany and Patrick Johnson, summer student intern, University of California, San Diego. In addition, the suthors would like to thank the personnel at the commercial vendors involved in grating fabrication work: Dan Cifelli and Elroy Pearson at Wasatch Photonics and Doug Smith and Plymouth Gratings Laboratories.

Nomenclature

a	avalanche ionization coefficient
A	area
AOI	angle of incidence
AR	Anti-Reflection
CPA	Chirped Pulse Amplification
d	layer optical pathlength
D	ideal layer thickness in a strictly transmission VPG
DCG	Dichromated Gelatin
η	Single-pass grating diffraction efficiency
E	energy
F	fluence (energy per unit area)
fs	femtosecond (10^{-15} s)
FWHM	Full Width at Half Maximum
HR	High-Reflection
J	Joule
λ_0	central use wavelength
λ_e	exposure wavelength
Λ	grating period
LIDT	Laser-Induced Damage Threshold
LLNL	Lawrence Livermore National Laboratories
m	diffracted order
mJ	milliJoule (10^{-3} J)
μm	micrometer (10^{-6} m)
MLD	Multi-Layer Dielectric
MPI	Multi-Photon Ionization
n	index of refraction
n_0	average index of refraction
Δn	change in index of refraction (i.e. amplitude of modulation about average n_0)
N_e	electron number density
nm	nanometer (10^{-9} m)
ns	nanosecond (10^{-9} s)
PW	PetaWatt (10^{+15} W)
ps	picosecond (10^{-12} s)
R	reflection coefficient
θ_0	angle of incidence at a material with respect to surface normal
θ_e	angle of incidence for grating exposure with respect to surface normal (general terms)
$\theta_{1,2}$	angles of incidence for grating exposure with respect to surface normal
θ’	angle of diffraction at a material with respect to surface normal
SNL	Sandia National Laboratories

t	true layer thickness
T	4-pass grating transmission
TW	TeraWatt (10^{+12} W)
VPG	Volume Phase Grating

Introduction

Short pulse lasers have undergone a rapid growth both in capability and application since the advent of chirped pulse amplification (CPA) in the mid-1980's [1]. In this approach, a short laser pulse is temporally stretched in order to reduce the peak intensity and to mitigate potential damage before amplifying it. After amplification, the pulse is then temporally re-compressed to nearly its original pulsewidth. Since such an approach to laser pulse generation uses dispersive elements in temporal compressors (see Fig. 1), grating technology has become essential. The largest CPA systems are petawatt-class systems capable of several hundreds of Joules in several hundreds of femtoseconds such as the now-defunct LLNL Petawatt system in the U.S. [2,3], the University of Osaka system in Japan [4], and the Rutherford-Appleton Laboratories system in the U.K., as well as a variety of planned systems. Such systems typically use gold relief gratings of meter scale in the temporal compressors [3]. The limitations are the relatively poor damage threshold (<0.5 J/cm^2), the efficiency (<95%), and the fabricated size available (< 1meter diameter) [2,5,6]. Such issues keep energies <1 kJ and thus limit peak intensities on the order of 1 PW.

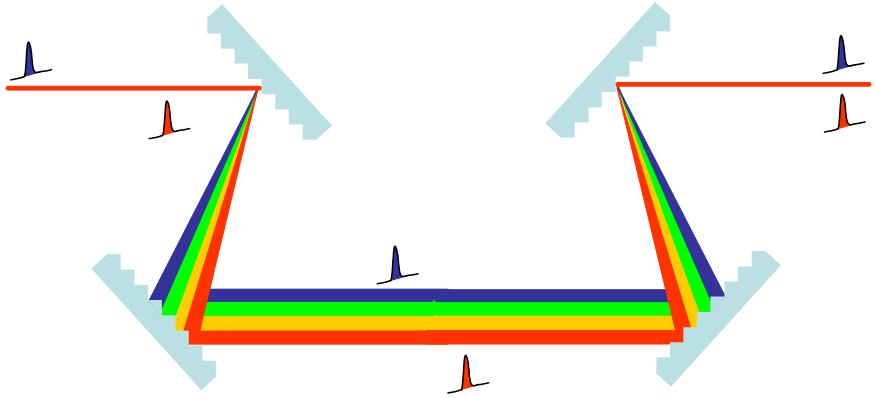

Figure 1. A conceptual grating compressor. The amplified and chirped input laser pulse will have the "bluer" or higher frequency components arriving after the "redder" or lower frequency parts. Dispersion in the compressor gratings causes the different frequencies to experience different pathlengths, eventually allowing the various spectral components of the pulse to exit synchronously. This re-compresses the pulse temporally. Two gratings can be used to compress a pulse but the beam will exit with a spectral spread in one dimesion. As such, 4 gratings (as depicted) in single-pass or 2 gratings in double-pass configurations are typically used.

In order to reach higher laser peak powers, one must either develop shorter pulse systems (<500 fs) at a fixed high energy using the available grating damage thresholds or one must increase the laser energy at a fixed short

pulsewidth (say ~500fs) by improving these damage thresholds. Since one planned application of short pulses at our facility (Sandia's Z-Beamlet) involves Fast Ignitor research [7,8], laser design necessitates multiple kilojoules of energy in a few picoseconds pulsewidth. As such, the technical problem at issue here is the development of improved grating technology (higher damage threshold and efficiency, yet scalable to large-aperture).

The existing damage threshold and efficiency are tied heavily to the material properties of gold in the grating. The small absorption of the metal leads to a lower damage threshold and lower efficiency than one might expect for a dielectric grating. As such, there is a push within the short pulse community to develop multilayer dielectric gratings [9-13]. While the designs may vary, the basic premise is to have an etched relief grating (often in silica) directly on top of a multilayer dielectric (MLD) mirror. Such systems offer the potential for much higher efficiencies (>95%) and improved damage thresholds (>1 J/cm^2) [11]. The latter improvement in part is due to the ability to mitigate electric field enhancement in groove structure. With the MLD gratings, the electric field penetrates into the material some, but proper design can push the fields more into the groove space than the material [10]. While such improvements are quite significant, the problem of large-aperture fabrication (which is greatly affected by the need for uniform etching) still remains. Due to the durability of the uppermost dielectric layers, wet chemistry/wet etch methods once used on larger gold gratings do not directly carry over to the newer MLD technology. Rather ion etching or reactive ion etching are preferred to maintain etch rates but, until recently, the need for such capability at larger apertures has not existed. As such, the development and certification of etchers with >50cm capability is a research area in itself.

A simple and elegant alternative to traditional gratings may be to develop gratings written in gelatin thin films. Sol-gel films can exhibit the requisite high damage-threshold (>10 J/cm^2 for 1 ns-scale pulses) [14,15] and can have gratings written into them [16-18], although verification of both properties simultaneously has not been explored. We propose coating a high damage-threshold mirror (>10 J/cm^2 at the ns-scale) with sol-gel and then writing a volume phase grating into the medium (see Fig. 2). Volume phase gratings (VPG's) essentially create a periodic index modulation and can exhibit very high efficiencies (>99%) [19]. To get such efficiencies, they are traditionally used in transmission. Often these gratings use a thin layer of gelatin material to create the grating and then seal the gelatin grating between two anti-reflection coated glass substrates for support and environmental protection. The glass thickness in transmission poses a problem for short pulse lasers due to B-integral effects, wherein the accumulated nonlinear phase due to the nonlinear refractive index of a bulk medium leads to small- and large-scale self-focusing and nonlinear optical damage as well as difficulties in pulse compression. In spite of this, such transmission gratings, as formed in Dichromated Gelatin (DCG) between glass plates, have been used at small scale for pulse compression but were ultimately

limited by nonlinear optical effects or damage in the glass substrate [20-21], with one source [20] indicating that the damage threshold at least exceeded the threshold for continuum generation (1 TW/cm^2 or 85 mJ/cm^2) in the grating substrate.

The use of the mirror as a backing eliminates nonlinear phase accumulation (B-integral) in the substrate leaving only the negligible phase accumulation in the thin grating layer. The environmental protection created by the glass cover would be gone but, in a vacuum environment (such as those typically used on larger peak power grating compressors), the problem would bypassed. Note that, since the substrate is a mirror, this periodic structure will constitute a double-pass transmission VPG, with the whole structure acting like a reflection grating. The suggestion of mirror-backed VPG's (again in DCG) has been made before for telecommunication applications [22-25] but has not been applied to pulse compression. The issue then would be to verify that the behavior of the mirror-backed VPG meets the needs of a petawatt laser system's grating compressor.

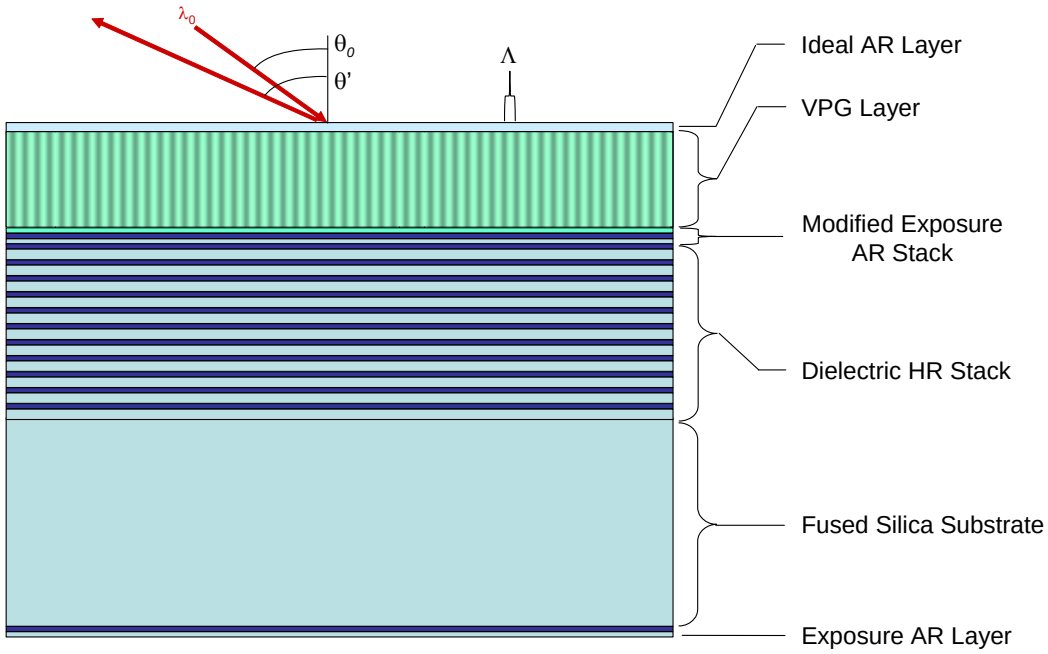

Figure 2. A conceptual mirror-backed volume phase grating. Unless labeled, layers apply to the central operating wavelength λ_0. For the VPG layer, the grating period is Λ, which diffracts incident light at λ_0 at an angle of θ_o (with respect to a surface normal) into an exit angle of θ' according to the standard grating equation: $(m\ \lambda_0/\Lambda) = (\sin\theta_o - \sin\theta')$, where m is the diffracted order.

2. Grating requirements

The petawatt grating compressor should meet the following criteria:

1) *Appropriate dispersion*. The grating dispersion should be high enough that the separation of the two gratings in the compressor is of a reasonable length (i.e. not exceeding 10m) due to the need for a vacuum housing vessel (see criteria 5 below). Based upon this, reasonable values are needed for the line spacing (i.e. the features are not too small for fabrication and yet are small enough to allow significant dispersion) and use angle (i.e. the angle for a Littrow or near-Littrow configuration does not require an excessively large grating). Historically, grating compressor designs have grating separations from 3 to 10m range, grating line densities from 1200 lines/mm to 1740 lines/mm (for groove periods/feature sizes of 570 to 830nm), and incident/use angles from 30 to 75°.

2) *High grating efficiency.* In common double-pass grating compressors for CPA lasers, a total of 4-reflections occur from the gratings. Thus, the total transmission T through the system is just the single-incidence first-order diffracted efficiency η raised to the fourth power ($T=\eta^4$), resulting in 65.6% transmission for η=90%. Thus compressor gratings must then exhibit reflection efficiencies η>90% to have acceptable losses. The nonlinear dependence is dramatic and good gratings should have η>95%, allowing total transmissions T>81%.

3) *High damage threshold.* Damage threshold issues are probably the most important for compressor gratings. Beam areas of 1000 cm^2 to 1500 cm^2 with a damage threshold fluence of 0.4 J/cm^2 (as for a gold relief grating) limits the output to 400 to 600 J. This limitation is based upon the use of gold gratings, which exhibit the fairly flat damage threshold of 0.4 J/cm^2 with respect to the laser pulsewidth for pulses in the 0.1 ps to 200 ps regime [26]. By comparison, dielectric materials exhibit a damage fluence threshold which increases with puslewidth, with the damage threshold almost always being higher than for metals. For a nominal 500 fs, damage threshold of fused silica is about 2.0 J/cm^2, which would then represent an upper limit for any reasonable silica-based MLD grating in this regime. The damage threshold improves to around 3.0 J/cm^2 at 5 ps duration. The potential for such an improvement in damage threshold and ensuing increases in laser output energies, in conjunction with higher diffraction efficiencies, is a large motivator for MLD grating development.

4) *Large-aperture capability.* The grating should be able to be fabricated at least to the 1 meter scale. The ability to achieve this may also involve realizing sufficient optical uniformity at large aperture (i.e the diffraction efficiency is uniform to within ±15% and the optical wavefront is uniform to within $\lambda/4$ peak-to-valley). Sol-gel coatings have been demonstrated up to fairly large apertures. For example, laser amplifier blast shields of size 1.8m

x 0.6m for the French Laser Mega-Joule project have been anti-reflection coated with sol-gel [27]. DCG diffractive optics are commercially available up to the 40 cm size. The associated coating processes are reasonably scalable and are highly cost effective when compared to the expense of large hard dielectric coating chambers. In addition, the VPG approach avoids any costs and scalability issues associated with large etching chambers. Wet etch or chemical rinse options can still be applied and maintain scalability in both the VPG scenario as well as harder gratings.

5) *Vacuum compatibility.* Due to the propagation distances involved, a petawatt-class laser accumulates a significant B-integral just from propagation in air. As such, the standard grating compressors and subsequent propagation paths and target areas must be in vacuum. Sol-gel's have seen extensive use in vacuum systems, particularly in vacuum spatial filters on high energy lasers. When not in vacuum, the damage threshold and reflectivity become affected by water vapor and contaminants. DCG suffers similar environmental problems and has also been used in vacuum settings. This lack of robustness is part of the reason that such VPG's may not be considered as a viable option to MLD's and gold-style gratings. This reasoning has certainly been used with regards to photoresist gratings [10]. However, the key here is to recall that, in any general high energy laser system, the environmental factors must be controlled anyway to mitigate damage. In addition, in a petawatt-class laser, the compressor is in vacuum, which automatically reduces the fear of dust contaminants and water vapor.

In addition to all of these physical needs, one would hope that the grating would be cost effective. We will address how each of these needs is met in principle by a mirror-backed volume phase grating. Manipulation of the key variables (grating period, use angle, the achievable index change, and gelatin layer thickness) should lead to gratings with both high efficiency and high damage-threshold at large-aperture. To enable a mirror-backed VPG to meet these needs requires us to know the approximate compressor design. As a nominal baseline, consider the design used in the LLNL petawatt laser. For that system, a 100 fs seed pulse at 1053 nm is stretched to 3 ns before amplification, setting the chirp. The compressor to compensate this chirp uses two 94 cm gold gratings with 1480 lines/mm at an 8.4 m spacing in a single-pass configuration [2]. The angle of incidence would have been 46.2° such that the output was 10.7° away at 56.9°, although the Littrow angle (the angle at which the first diffracted order is anti-parallel to the incident beam) is actually 51.2°.

3. Grating design

To design the grating, one must keep in mind the compressor grating requirements outlined in section 2. We have chosen to model the scenario using GSolver, a commercial grating design program [28], in order to consider

multiple effects,. As input parameters, we need to know reasonable values of the bulk refractive index of the grating. Chemistry allows one to adjust the refractive index of silica sol-gels from 1.22 to 1.44, with around 1.22 being common for anti-reflection (AR) coatings of BK7 and fused silica [15]. Similarly, DCG's refractive index can be adjusted from 1.27 to 1.54 [29]. As a reasonable value for both, we consider an average bulk index of n_0=1.35. We then consider the index modulation Δn in addition to that. A value of Δn=0.06 for n_0=1.35 refers to $n=n_0 \pm \Delta n/2$, allowing n to vary from 1.32 to 1.38. To date, Δn's in sol-gel have only reached 0.02 [17] while they have reached 0.25 in DCG [29]. For the average n_0=1.35 considered, we will only consider values of Δn up to 0.2, since this is an acceptable value for DCG (although it requires a great development leap on the part of sol-gel).

Since the phase shift and hence the optical pathlength is critical in the grating, one must consider the optical thickness of the VPG. Sol-gels have been coated beyond 20μm thickness, but the uniformity over a large aperture is a problem. For most practical optical applications, sol-gel coatings are kept to less than 1μm in order to maintain coating quality. DCG can coat up to 100μm thickness but it is more common to see 5 to 20μm films (with 10% variation from edge to center) for optimal efficiency transmission gratings [29]. The general uniformity concerns imply that it would be best to minimize the thickness. For a 10% variation to stay less than a wavefront distortion of λ/2 (to maintain a decent wavefront in the beam) and a wavelength λ of 1053nm, the desired thickness would be around 5μm for DCG.

As a starting point, we consider a mirror-backed grating of 1480 lines/mm (675.675nm period) to look at the effective operation of the concept. Similarly, we start by considering a Littrow configuration (θ_0=51.2° incidence), as well as the more complex off-Littrow incident angle of 46.5° and exit angle of 56.5°. Since the anticipated bandwidth (FWHM) of short-pulse Nd:Glass laser systems is about 5nm centered at 1053nm, we should consider use wavelengths in a slightly larger band from 1048 to 1058nm to make sure that the spectral wings are covered. The grating layer is considered to be uniform throughout the thickness of the layer (i.e. there is no decrease in index modulation with depth) and is created by a sinusoidal variation in the refractive index from $n_{min}=n_0 - \Delta n/2$ to $n_{max}=n_0 + \Delta n/2$.

Based upon use angle and average grating layer bulk refractive index, a mirror design is established. The same issues discussed on mirror design for MLD gratings should apply. Thus, the mirror should have an optimal reflection for the use wavelength and use angle and should be nearly fully transmissive at the exposure wavelength and exposure angles. A standard quarter-wave stack of high and low index materials is chosen for the mirror, following the general design that:

$$n_H d_H = n_L d_L = \lambda_0/4 \quad (1)$$

where n is the refractive index, d is the optical pathlength in the material, and λ_0 is the vacuum wavelength of the incident light, with the H and L subscripts referring to high and low index respectively. Note that the pathlength d is the true layer thickness t times $\cos\theta_0$ for the angle θ_0 formed between the surface normal and the optical beam. Typically, s-polarization is favored for the grating mirrors since MLD gratings have the best diffraction efficiency for the thinnest layers when used in s-polarization (TE mode). However, while thin grating layers are easier for some situations, other situations may favor a thicker grating and the use of p-polarization. As such, both scenarios have been explored.

Note that the reflection oscillations at lower wavelengths might cause a significant reflection at the exposure wavelength, leading to a ghost structure in the grating. As such, we must consider the exposure wavelength and angle of incidence. For a grating of period Λ and an exposure wavelength λ_e,

$$\Lambda = \lambda_e /(2\cdot\sin\theta_e\cdot\cos\phi) \quad (2)$$

where the angle θ_e is the half-angle between the two exposing beams and ϕ is the angle of any small deviation that the grating surface normal might have with the axis of symmetry between the two exposing beams (see Fig. 3) [11]. For non-zero ϕ to prevent back-reflections, the two beams will have slightly different incident angles θ_1 and θ_2. Some common exposure wavelengths and angles are tabulated in Table 1.

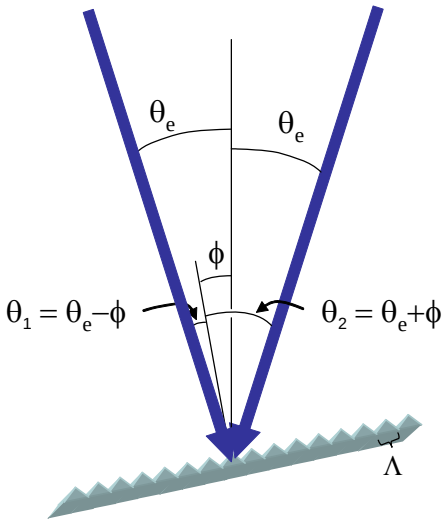

Figure 3. Grating exposure arrangement.

Table 1. Exposure conditions to achieve Λ = 675.675nm (1480 l/mm).

λ_e (nm)	ϕ (°)	θ_e (°)	θ_1, θ_2 (°)
355	0	15.23	15.23, 15.23
	2	15.24	13.24, 17.24
413	0	17.80	17.80, 17.80
	2	17.81	15.81, 19.81
488	0	21.17	21.17, 21.17
	2	21.18	19.18, 23.18
532	0	23.18	23.18, 23.18
	2	23.20	21.20, 25.20

Some groups have had the problem that the third harmonic peak at 351 nm can shift up when the incident angle changes, causing higher reflections at a λ_e =413 nm (as seen in Fig.4). The proposed solution in mitigating these reflections was an elaborate modification to the mirror structure [10]. Another solution is to use a slightly higher wavelength such as λ_e =488 nm. If these were simple Fresnel reflections from the mirror, one would suggest an anti-reflection coating at λ_e on top of a slightly modified mirror. As such, we chose to add a few more anti-reflection layers to the top. Furthermore, any real mirror used for this application would also have its rear surface AR coated at 488 nm to prevent ghost structures in that grating from that source.

Based upon the discussion of grating needs and exposure, one arrives at a mirror design goal for a high reflector (R>95%) at wavelengths from 1045 to 1060nm for the use angles from 45 to 60°. Similarly, the grating exposure dictates that the mirror should be a high transmitter (R<1%) for 488nm from 15 to 30°. Designs will be considered for both s- and p-polarizations.

3.1 S-polarization Designs

3.1.1 S-polarization Mirror Designs

Due to the broader use of s-polarization for high efficiency thinner layer MLD gratings, this scenario was considered first. For the best damage thresholds in the MLD stack, we choose HfO_2 as the high index material (n_H=1.8879) and SiO_2 (n_L=1.4498) as the low index material. For λ_0=1053 nm and θ_0=51.2° incidence, the angles in the media are θ_H=24.38° and θ_L=32.52°, resulting in layer thicknesses of t_H=153.09 nm and t_L=215.35 nm. Eleven such high-low pairs (or 22 total layers), represented as $(HL)^{11}$, give high reflection at 1053 nm and at 51.2° angle of incidence, with the reflection being >99.5% for s-polarization and lower for p-polarization (See Fig. 1). Note that Fig. 5 indicates a broad reflection minima of about 1% or less for the exposure angles of interest.

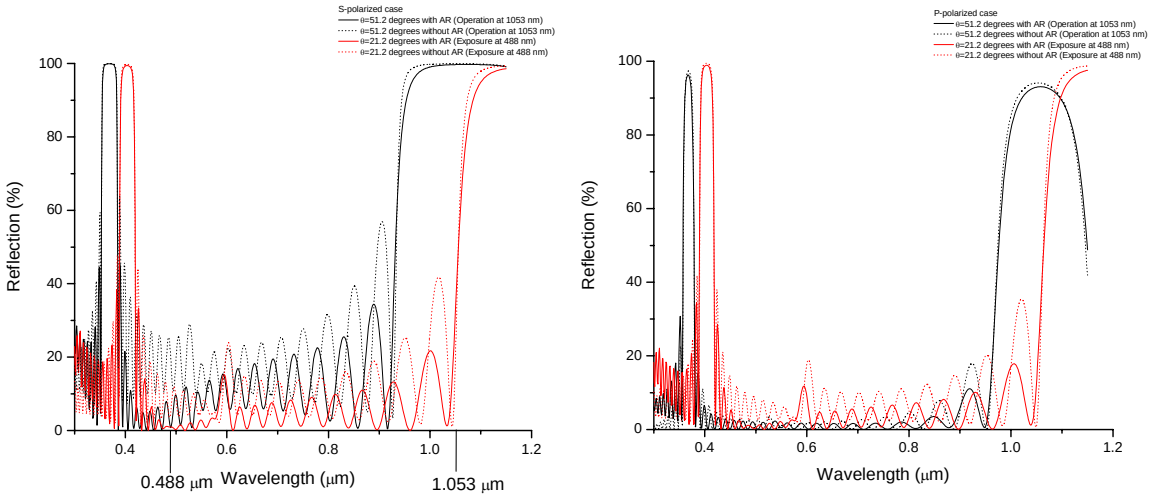

Figure 4. (Left) Reflection efficiencies for an $(HL)^{11}$ multilayer dielectric mirror design used at s-polarization. The solid black curve is the nominal high reflector at 1053 nm and 51.2° incidence. The solid red curve verifies the mirror operation at 488 nm and 21.2° incidence. Dashed curves are without the empirically derived anti-reflection layers. (Right) The same mirror used in p-polarization.

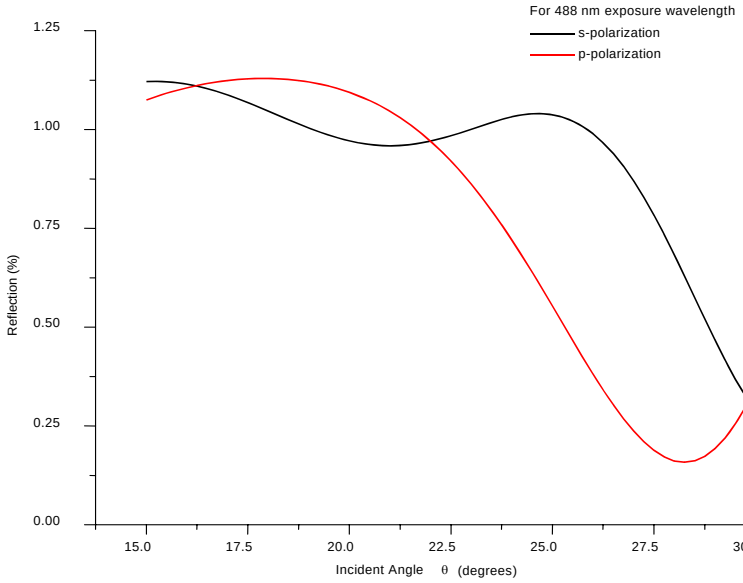

Figure 5. Reflection efficiencies at 488 nm for s- and p-polarizations near the illumination angle of 21.2° incidence.

3.1.2 S-polarization Grating Designs

Upon this multilayer stack, one can now model a volume phase grating. We first look at the effect of grating layer thickness upon diffracted efficiency for a fixed refractive index modulation Δn. This shows a slowly varying sinusoid with high amplitude, high frequency modulation on top (see Fig. 6). The modulation is due to etalon effects in the grating layer itself. In fact, a Fourier transform of the data

shows that the subtle beating of the high frequency modulation is actually due to the two different index extremes ($n_{min}=n_0 - \Delta n/2$ and $n_{max}=n_0 + \Delta n/2$) in the grating. One benefit of using the more rigorous modeling software rather than a simple analytical model like that of Kogelnik [19] is to point out unexpected results like this etalon behavior.

Due to these etalon-effects, the grating surface was given an idealized anti-reflection (AR) coating. For known refractive indices in air and the bulk VPG medium (n_0=1.0 and n_{VPG}=1.35 respectively) as well as angles (θ_0=51.2° and θ_{VPG}=35.26°), the refractive index of an idealized single-layer AR can be determined to be n_{AR}=1.1393 by setting equal the Fresnel reflectivities from air into the AR and from the AR into the VPG. With a known index and corresponding angle in the media (θ_{AR}=43.16°), a quarter-wave thickness of t_{AR}=316.7 nm is determined. Such a structure could be a simple coating of an aerogel or modified sol-gel AR. With this AR applied in the model, the etalon-generated structure is basically eliminated (see Fig. 6). The residual ripples may be due to the index modulation of the grating where the index extremes are not effectively matched.

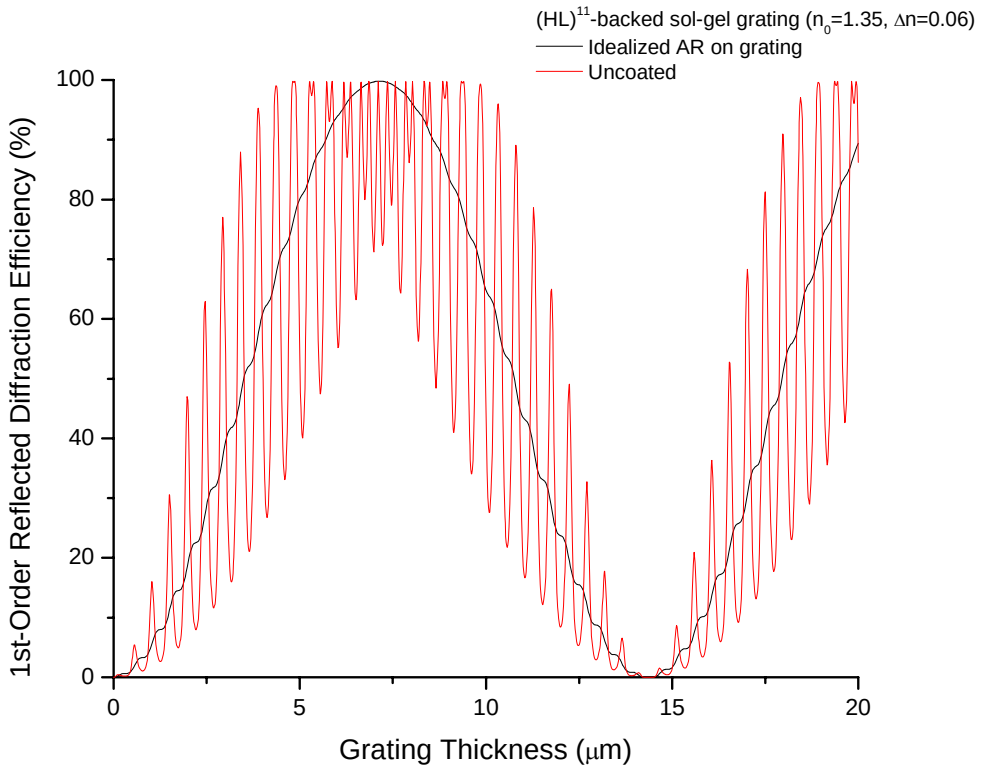

Figure 6. First order diffraction efficiency at 1053 nm for s-polarization at 51.2° incidence versus VPG layer thickness.

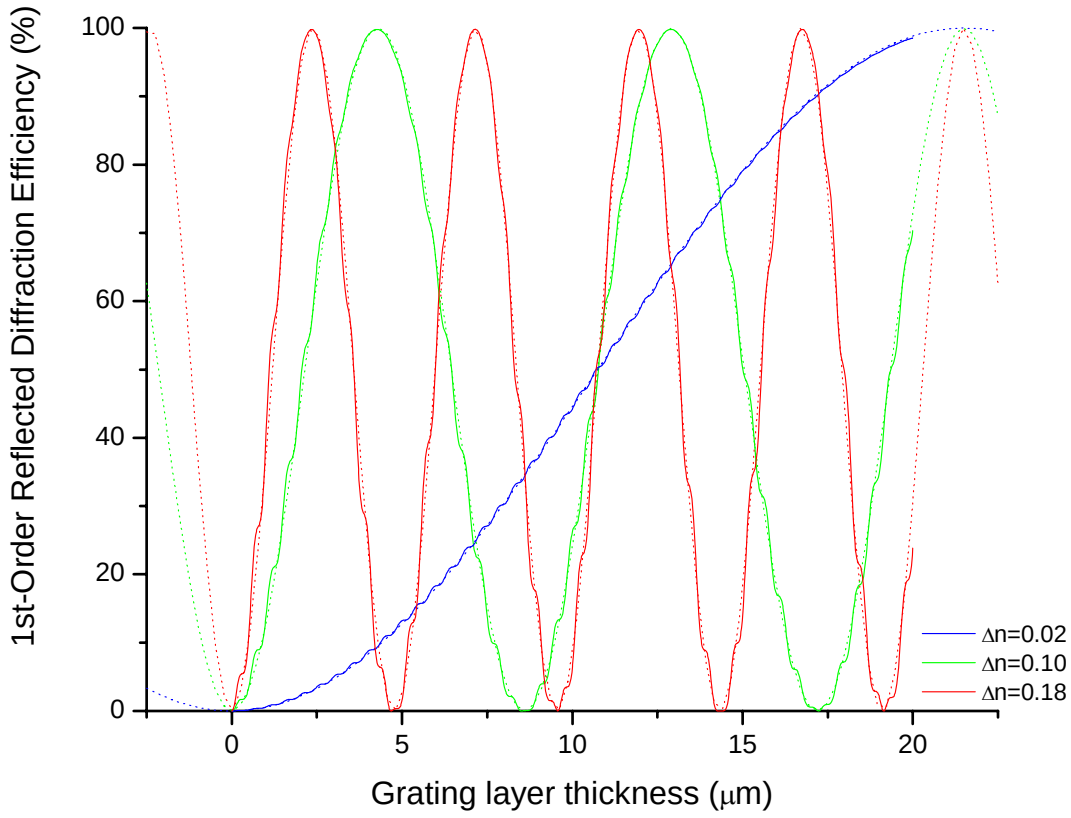

Figure 7. First order diffraction efficiency (at 1053 nm for s-polarization at 51.2° incidence) versus VPG layer thickness for different Δn (0.02, 0.10, and 0.18) and n_0=1.35. The grating here is a sinusoidal index modulation. The simulation data is represented in the solid lines while the simple Kogelnik theory is represented by the dotted curves.

Including the AR in the model, the original idea of varying the thickness and Δn was examined for a sinusoidally varying volume phase grating backed by our high reflector (see Fig. 7). The modeled curves are overlaid with a simple theoretical curve for a non-absorbing dielectric transmission VPG presented by Kogelnik [19]. In Kogelnik's theory, the transmitted diffraction efficiency η for a lossless dielectric grating structure of thickness D with an internal beam angle of θ in the medium and a slant angle ϕ of the grating with respect to the substrate is:

$$\eta=\sin^2\nu \qquad (3)$$

where, for s polarization,

$$\nu_S = \frac{\left(\left[\pi \cdot \Delta n \cdot D\right]/\left[2 \cdot \lambda_0\right]\right)}{\sqrt{\cos^2\theta - \left[\lambda_0 \cdot \cos\theta \cdot \cos\phi\right]/\left[n_0 \cdot \Lambda\right]}}. \qquad (4)$$

This condition holds exactly if the Bragg condition is satisfied:

$$\sin \theta_{VPG} = \lambda_0/(2n\Lambda) \qquad (5)$$

In our case of λ_0=1053 nm, n_{VPG}=1.35, and Λ=675.7 nm (1480 lines/mm), θ_{VPG}=35.26° satisfies the condition.

Based upon this, the only assumptions for the mirror-backed VPG are that the grating fringes are orthogonal to the mirror surface (i.e. the grating fringes are unslanted or ϕ=90°) and that the theoretical grating layer thickness t is exactly half that required for a thick film Bragg transmission grating in Kogelnik's standard approach (i.e. t=D/2). The first condition is the simplest means to satisfy the Bragg condition. The second condition is consistent with Kogelnik's model being for a single-pass transmission grating whereas our model concerns a double-pass mirror-backed VPG. As seen in Fig. 7, the theory matches well, showing that in this respect the mirror-backed grating option performs like a modified Bragg transmission grating and can exhibit a theoretical efficiency of η>99%. Note that Eq. 3 points out that the efficiency will peak when $\nu=\pi/2, 3\pi/2$, etc. or when $\Delta n \cdot t = \lambda_0 \cdot \cos\theta_{VPG}/2$ = 0.43, 1.29, etc. These peaks trace out a series of curves indicated by the white bands of the contour plot in Fig. 8. Such efficiency peak curves show that, for reasonable Δn<0.2, the grating layer thickness cannot be less than 2 μm.

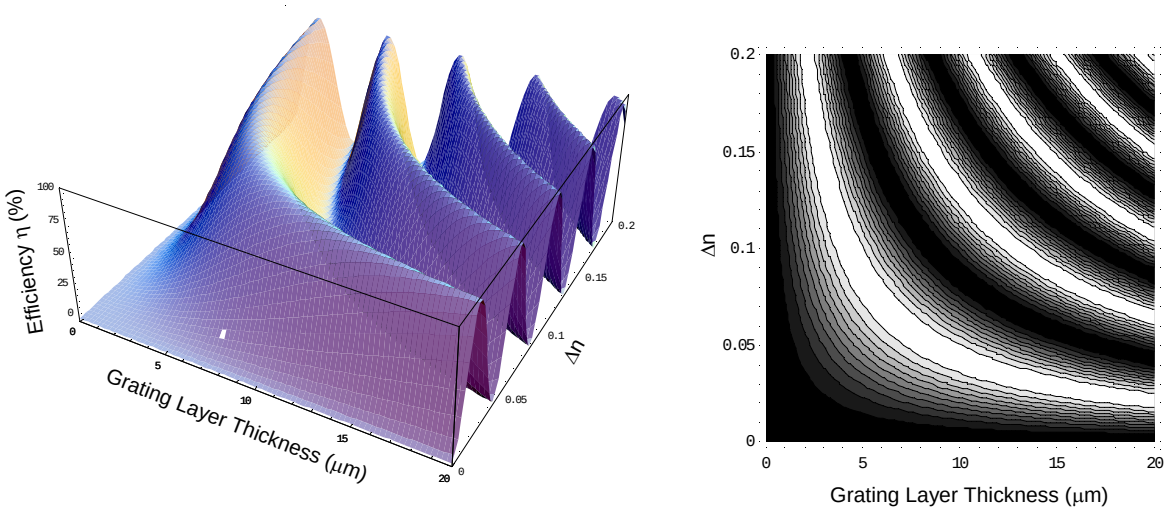

Figure 8. (Left) A 3D plot of the simple Kogelnik theory showing where efficiency peaks as a function of grating thickness t and index modulation Δn. (Right) A top view contour plot with the white bands representing peak efficiencies.

For a few such optimal sets of Δn and t, the efficiency as a function of wavelength and incident angle is examined (see Fig. 9). As one can see in the figure, the bandwidth increases as the thickness t decreases and the index change Δn increases. Similarly, the acceptance angle increases as the thickness t decreases and the index change Δn increases. To quantify a bit, consider the spectral and angular ranges of desired operation, which we would like to be η>95%. The associated widths are plotted versus Δn in Fig. 10. The basic result indicated is that the bandwidth $\Delta\lambda$ is more than sufficient for a >100fs scale chirped pulse system but the angular acceptance $\Delta\theta$ is relatively narrow, specifically too narrow to use this design (the straightforward case where the grating fringes are orthogonal to the substrate) in the off-Littrow configuration (which would require $\Delta\theta$>[51.2°-46.5°]=4.7°).

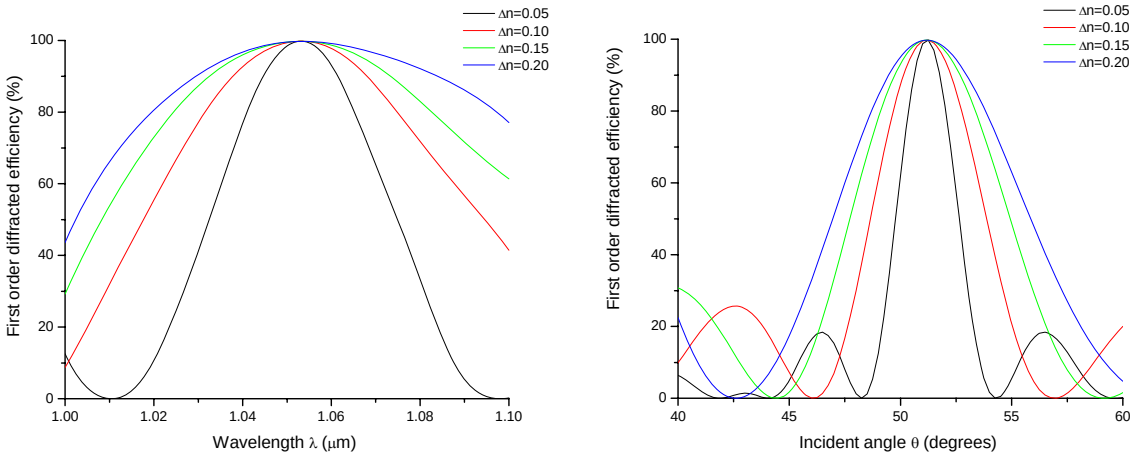

Figure 9. (Left) Efficiency η versus wavelength λ for optimal grating thickness t and corresponding index modulation Δn pairs. (Right) Efficiency η versus incident angle θ for optimal grating thickness t and corresponding index modulation Δn pairs.

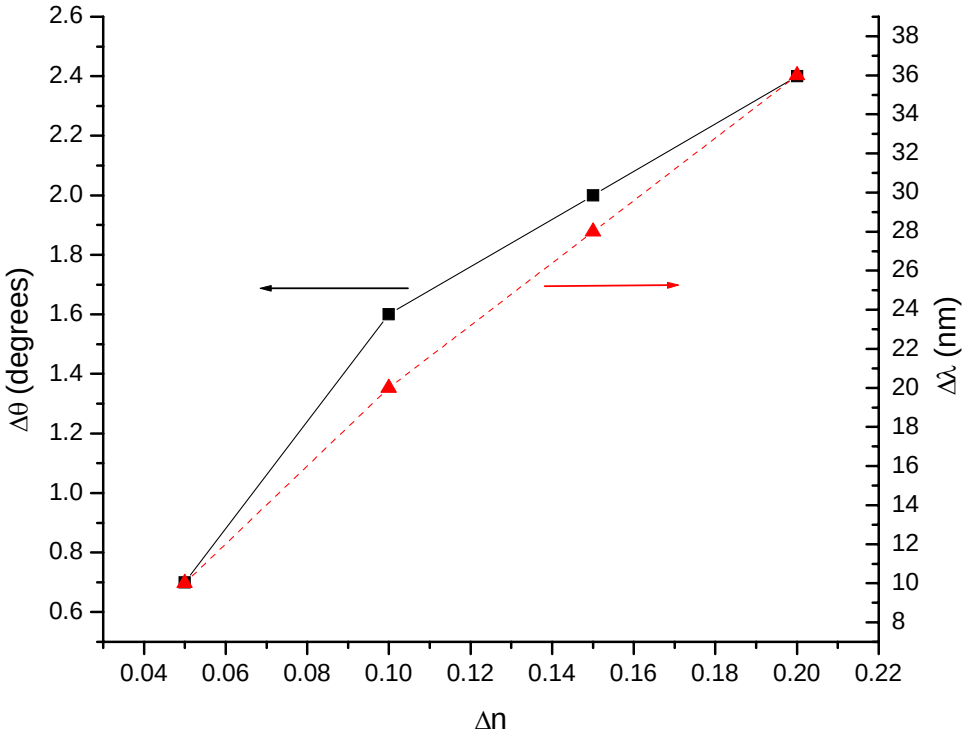

Figure 10. Bandwidth Δλ versus Δn (in red) and acceptance angle Δθ versus Δn (in black) for optimal grating thickness settings in Figure 6.

In addition to all of the design validation, the first year of the LDRD hoped to model the effects of field enhancement in the grating structure. Such work was done by Bill Johnson and company in Org. 1642 using a modification to existing Sandia electromagnetic codes. These modifications were benchmarked against existing published data on multilayer dielectric gratings [2] with nice agreement (see Fig.11). The code was then applied to the baseline design of the mirror-backed grating. An electric field map of the results (for a single grating period) show a high field enhancement inside the grating structure (see right side of figure). A similar model run for a gold-backed grating shows a similar field enhancement higher up in the grating (see left side of figure). This data points out some key issues. First, the field enhancement is located a fixed distance of roughly half of one optical wavelength from the surface of the high reflector, whether it be a multilayer dielectric structure or gold. The reason for the difference in the two cases is that, in the multilayer case, there are a few extra dielectric layers for AR purposes above the final surface of the mirror. The net result of such field enhancement placement is that one is driven again towards very thin gratings and higher index modulations. The other point is that the field enhancement can be made to lie almost entirely within the grating structure (as indicated in the left figure gold-backed grating case). Since damage thresholds

are typically higher in bulk media than at a dielectric interface, the result of a high field enhancement may not be such a problem. Only correlated damage testing will verify this.

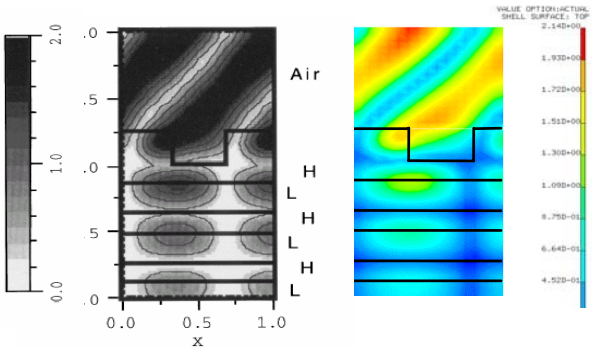

Field modeling in Shore, Perry, et al **JOSA A** v.14 n.5 (May 1997)

Field modeling benchmark of Shore data by Johnson and Coats (s-polarization)

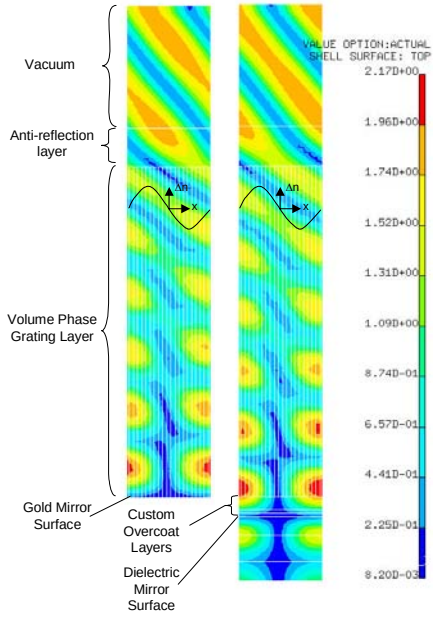

Figure 11. (Top) Benchmarking: Upper left- Field modeling of an etched MLD grating from [10], Upper right- SNL benchmarked model of the same grating from [10]. (Bottom) Application to SNL mirror-backed VPG for case of s-polarization and grating fringes normal to mirror (n=1.35, Δn=0.16, t=2.688μm): Bottom left- Gold-mirror backed case Bottom right- Dielectric mirror-backed case.

3.2 P-polarization Designs

3.2.1 P-polarization Mirror Designs

As design work evolved, discussions with makers of DCG volume phase gratings began in order to prototype the concept. The main vendor concerns were the layer thickness (which was desired to be in the 5 to 20 μm range) and the use of an anti-reflection top-coat. For DCG production, an ideal aerogel AR is not possible and a standard dielectric hard coat may distort the delicate gelatin. As such, a bit of investigation suggested that, if the grating is designed and used at p-polarization, the fact that the grating use angle is so near to Brewster's angle (for which p-polarized reflections are minimized) may mitigate the strong etalon-effect from the gelatin layer seen with s-polarization [30] (see Fig. 6). To be clear, the Brewster's angle for n=1.4 is θ_0=ArcTan(n)=54.5° and for n=1.35 is θ_0=ArcTan(n)=53.5°, both of which are close to the 51.2° Littrow angle. This option was modeled with GSolver with the result that the etalon effect was mitigated as expected (see Fig. 12). With this in mind a design was created for a p-polarized mirror substrate.

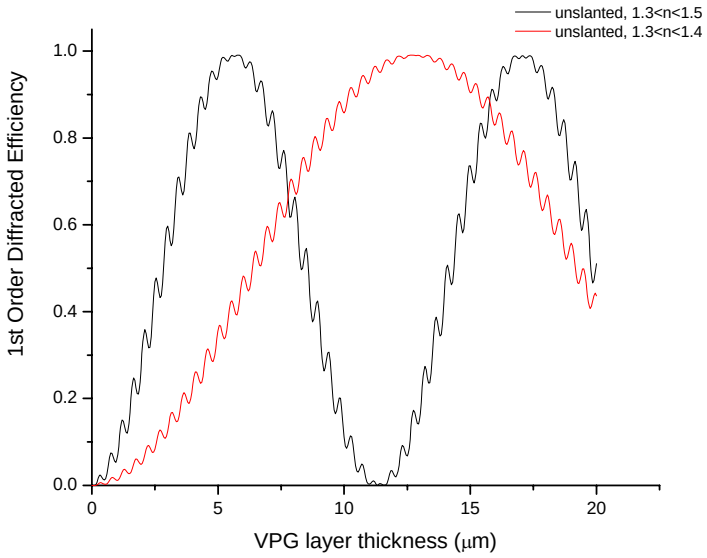

Figure 12. First order diffraction efficiency (at 1053 nm for p-polarization at 51.2° incidence) versus VPG layer thickness. In the unslanted case, the fringes/phase gratings are normal to the substrate.

The new MLD mirror was designed to be a high reflector for 1045-1060nm at a 45-60° angle of incidence (to accommodate the eventual grating requirements) while still being a high transmitter for 488nm from 15-30° angle of incidence (to accommodate the grating exposure). The latter issue requires an anti-reflection coating upon the rear surface for 488nm from 15-30° angle of incidence to continue ensuring that stray exposure light does not establish undesired secondary "ghost" grating structures. The original design called for a 34 layer (17

HL pairs) HR on the front substrate surface and a 2 layer AR on the rear surface. Samples of the experimental mirror design were fabricated with the help of Plymouth Grating Laboratories. The design goals and the measured spectral responses of the mirrors are both shown in Fig. 13. The figure shows that the fabricated mirrors match the design well, achieving high reflection for 1045-1060nm at 45-60° angle of incidence. The deviations from the design goal stem from several issues. For one, the vendor preferred a 4-layer AR due to material selection. In addition, the 34 layer design was quite thick at a combined layer thickness of 6.07 μm. The vendor had to cut out 4 layers (or 2 HL pairs) which marginally reduces the reflection efficiency. However, these two small adjustments as well as small deviations in the modeled versus real layer thicknesses and indices of refraction easily explain the small variation of the fabricated samples from the original design parameters.

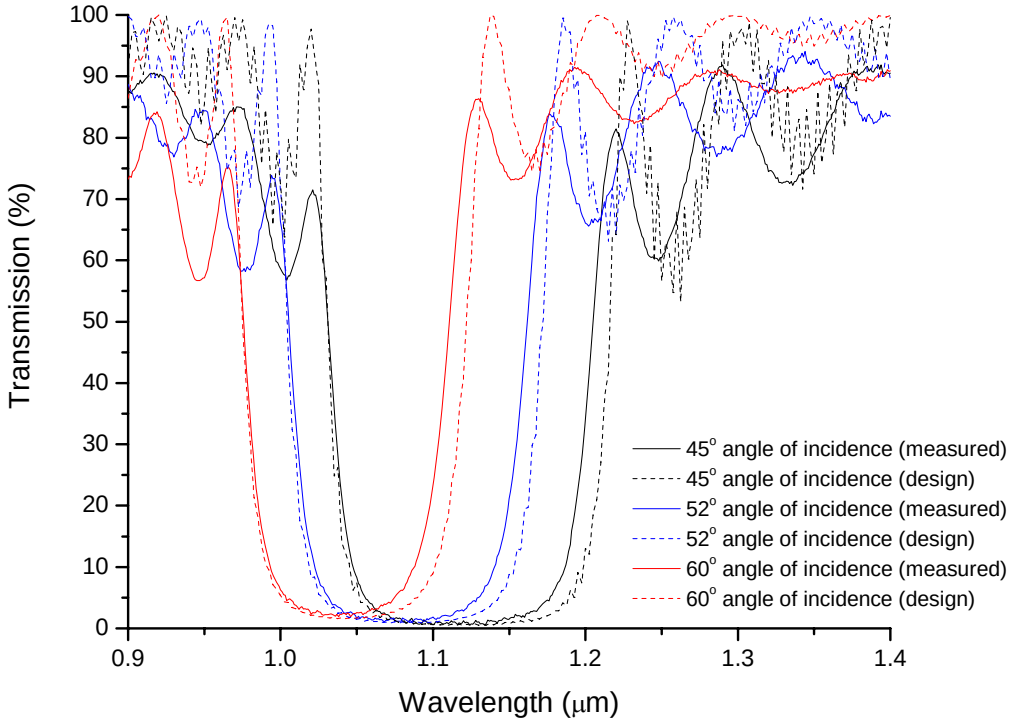

Figure 13. Dielectric coated mirror design goals and measured performance. Note that, since the plot shows transmission rather than reflection, the large transmission bands in the 1.0 to 1.2 μm spectral range correspond to efficient reflection in this range.

3.2.2 P-polarization Grating Designs

Analysis quickly indicated similar results to the s-polarized case with respect to bandwidth and acceptance angle. In general, reasonable $\Delta n \sim 0.2$ allow sufficient bandwidths $\Delta\lambda > 10$nm for $\eta > 90\%$ but keeps acceptance angles fairly narrow at $\Delta\theta < 3°$ for the same efficiency range. As such, slanted grating fringes (i.e. those

where the grating fringes are non-orthogonal to the mirror substrate or $\phi \neq 90°$) are considered.

In Kogelnik's theory [19], the grating efficiency for p-polarization is still the simple relation $\eta=\sin^2\nu$ from Eq. 3 as long as the Bragg condition is satisfied. However, the factor ν is modified for p-polarization:

$$\nu_P = \frac{\left([\pi \cdot \Delta n \cdot d]/[2 \cdot \lambda_0]\right)}{\sqrt{\cos^2\theta - [\lambda_0 \cdot \cos\theta \cdot \cos\phi]/[n_0 \cdot \Lambda]}} \cdot \cos[2 \cdot (\theta_0 - \phi)]. \quad (6)$$

The small deviation from the Bragg condition which will result for broadband pulses used with slanted grating fringes will cause the relation from Eq. 3 to become an approximation. Kogelnik's theory for the efficiency includes extra terms to account for deviations from the Bragg condition but the expression becomes quite cumbersome. However, as will be demonstrated, the relation expressed in Eq. 3 still holds up quite well as long as these Bragg deviations are small.

A sample comparison of the slanted versus unslanted cases appears in Fig. 14, which is the p-polarization analog to the s-polarized sample data in Fig. 9. To better clarify things, some key cases are summarized in Table 2. The Kogelnik theory was used to provide baseline information such as the layer thickness for the other given parameters which determine the peak efficiencies. Using these values, a simulation using GSolver was performed assuming a gold substrate at first to approximate the idealized case which Kogelnik represents. Afterwards, the MLD substrate design was added to the model. As seen in the layer thickness row of Table 2, the theory and modeled data agree well. In the model, the addition of the gelatin layer to the MLD substrate originally created some small percentage of 488nm reflections which were not present with the MLD mirror alone. This forced small changes to the gelatin layer thickness in order to mitigate any 488nm reflections (as indicated in the first two data rows of Table 2). The net result was a p-polarized DCG mirror-backed grating *design* (not prototype) with greater than 95% efficiency over >10nm bandwidth in each of the 4 cases. The use of slanted fringes does slightly reduce the peak diffraction efficiency available and increase the gelatin layer thickness. However, slanted fringes do permit the requisite angles of incidence and adequate bandwidth.

To validate the concept, the custom mirror samples received from Plymouth Grating Laboratories were sent to Wasatch Photonics for coating with DCG and subsequent exposure. Grating samples for case 3 described in Table 2 were not in fact created because the gelatin layer thickness was deemed too thick. However, six samples for each of cases 1, 2, and 4 were fabricated (see Fig. 15) and the results are shown Table 3. The best sample achieved as high as a first-order diffraction efficiency of η = 88% and numerous other samples achieved efficiencies in the 70-80% range. The other cases were unable to produce significant quantities of gratings with efficiencies greater than 50%.

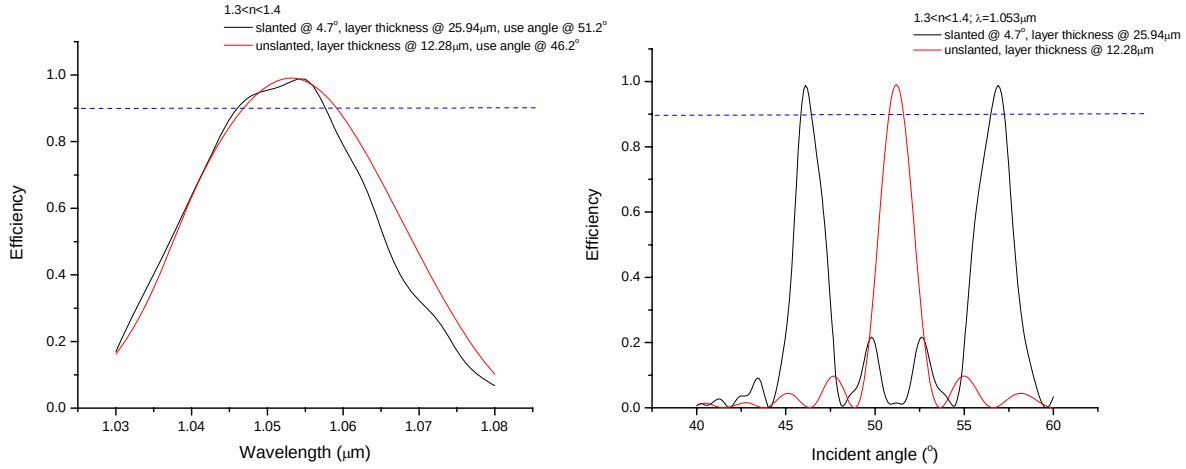

Figure 14. (Left) First order diffraction efficiency (for p-polarization at fixed use angles) versus wavelength for unslanted and sample slanted fringe cases. (Right) First order diffraction efficiency (at 1053 nm for p-polarization) versus incident angle for unslanted and sample slanted fringe cases.

Table 2. Fabrication considerations for p-polarized DCG gratings.

All gratings: Λ=675.675nm(1480 l/mm); 50%duty cycle (sinusoidal)	***Case1: AOI=51.2°(Littrow), 1.3<n<1.4, 1053nm design; n=1.4 unexposed, 488nm exposure at 21.2°***	***Case2: AOI=51.2°(Littrow), 1.3<n<1.5, 1053nm design; n=1.5 unexposed, 488nm exposure at 21.2°***	***Case3: AOI=46.2 °, 1.3<n<1.4, 1053nm design; n=1.4 unexposed, 488nm slanted exposure at 16.2°,26.2°***	***Case4: AOI=46.2 °, 1.3<n<1.5, 1053nm design; n=1.5 unexposed, 488nm slanted exposure at 16.2°,26.2°***
VPG layer thickness on gold (both Kogelnik theory and Gslover model) and adjusted for MLD (mm)	12.68 (K),12.68 (G) → *12.63 (G)*	5.75 (K), 5.75 (G) → *5.7 (G)*	25.94 (K), 25.94 (G) → *25.93 (G)*	10.17 (K), 11.6 (G) → *11.58 (G)*
Unexposed MLD 488nm reflectivity at exposure angles with original and adjusted gel layer (%)	*R<6.7%* → *R<0.13%*	*R<10.0%* → *R<0.14%*	*R<0.78%,3.6%* → *R<1.8%,2.5%*	*R<1.7%,2.7%* → *R<0.15%,0.36%*
Slant angle f (°)	0	0	4.7	4.8
η @ 1053nm @ 46.2°, 51.2°, and 56.9° (%) with gold mirror and with adjusted gel layer on MLD	0.15%,99.05%, 0.4%→0.11%, 98.32%,1.32%	1.07%,99.04%, 0.69%→11.61%, 98.39%,13.25%	97.91%,1.5%, 98.81%→96.94%, 3.09%,95.40%	98.93%, 5.29%, 99.01%→94.99%, 3.69%,95.64%
Acceptance angles and incident ranges (°) at 1053nm	0.8° (51.6°-50.8°)	1.8° (52.1°-50.3°)	0.5° (46.4°-45.9°); 0.7° (57.2°-56.5°)	2.1° (47.3°-45.2°); 2.7° (58.1°-55.4°)
Bandwidth and ranges (nm) at AOI	12nm (1059-1047nm)	28nm (1067-1039nm)	10nm (1057-1047nm)	35nm(1071-1036nm)

Table 3 Fabricated DCG grating results

	Case 1	Case 2	Case 4
First-order Diffraction Efficiency (and Sample Serial Number)	77% (S/N 347), 80% (S/N 393), XX% (S/N XXX), XX% (S/N XXX), XX% (S/N XXX), XX% (S/N XXX)	71% (S/N 314), XX% (S/N XXX), XX% (S/N XXX), XX% (S/N XXX), XX% (S/N XXX), XX% (S/N XXX)	88% (S/N 054), 82% (S/N 148), 81% (S/N 158), 84% (S/N 160), 82% (S/N 162), 72% (S/N 169)
Average Diffraction Efficiency (and Standard Deviation)			81.5 ± 5.3 %

Figure 15. (Left) DCG mirror-backed grating prototype from Case 2. The spectral dispersion observed indicates that the sample has some response in the visible wavelength band as well as the designed infrared region. (Right) DCG mirror-backed grating prototype from Case 4 after vacuum pump-down.

While the grating efficiencies are quite nice, the DCG layer is noticeably hygroscopic. While one does not directly see water accumulate on the gelatin film, one can see a drop in diffraction efficiency after several days of ambient atmosphere exposure. The attempt was made to pump down such a mirror-backed VPG sample in a vacuum cell to draw off the water. In general, such a maneuver does not harm DCG films on fused silica substrates with no MLD mirror stack, as was verified. However, the presence of the thick HR MLD stack complicates the overall structure and the mirror-backed VPG developed pronounced fine stress lines along with tearing of the films away from these stress lines (see Fig. 15). Dielectric films of HfO_2 and SiO_2 tend to show greater signs of stress when placed upon fused silica substrates than with other glass material substrates like BK7. These stresses are then exacerbated when the coated optic is placed in vacuum. Problems like this have been observed in

some etched MLD grating work where the coating began to craze and peel when placed in vacuum. While not all coated substrates have vacuum incompatibility issues, the issue of low stress coatings for vacuum applications is an on-going area of work in the optics community at large but the topic lies outside the scope of this research.

4. Damage Thresholds and Damage Testing

4.1 Theory of Damage

One of the core issues in optics development is the laser-induced damage threshold (LIDT). The data is typically quantified in terms of a damage fluence or energy per unit area (F=E/A) at a given pulsewidth. Electric field enhancement is known to be a problem in MLD studies because it can reduce the damage thresholds. Since damage thresholds tend to be lower at dielectric interfaces, it is believed that the effect can be mitigated in dielectric or volume phase gratings in part by trying to shift the high field regions to the air gap, by more generally placing the field enhancement in the bulk material (especially the low index material), or by distributing the field more uniformly via soft transition boundary condition. Beyond such considerations, grating damage becomes as much an issue of material science as of design.

With regards to basic material science and LIDT, lower density materials (like sol-gel) should benefit slightly from an inherently better damage threshold than the higher density counterpart (like bulk fused silica). To understand this, consider the mechanism involved in short pulse damage [31]. Avalanche Joule heating dominates in the long pulse regime (>100 ps) with a scaling dependence of τ^{α} for $0.4<\alpha<0.5$. For a temporal intensity profile I(t), the Joule heating follows a rate equation for electron density N_e growth with time t:

$$dN_e/dt = [a\, I(t)]\cdot N_e(t) \qquad (7)$$

The factor a is the avalanche coefficient. At shorter pulsewidths, multiphoton ionization (or even tunneling ionization for extremely high intensities) begins to become significant. The multiphoton ionization (MPI) for an n^{th} order process will follow a distinctly different rate equation:

$$dN_e/dt = N_0\cdot[\, \sigma\cdot I(t)^n] \qquad (8)$$

The net rate equation is the sum of these:

$$dN_e/dt = [a\, I(t)]\cdot N_e(t) + N_0\cdot[\, \sigma\cdot I(t)^n] \qquad (9)$$

From this, one can see that MPI will dominate the ionization early on but eventually the collisional/avalanche ionization rate will exceed the MPI rate, causing MPI to act as a seed for avalanche ionization. Eventually, the material achieves a plasma density equal to the critical density. Above this density, the

laser energy is strongly absorbed in the long pulse limit, leading to the common definition of the damage fluence as the fluence at which critical density is reached [31]. It is worth mentioning that, for shorter pulses, the plasma scale lengths become shorter than the laser wavelength, leading to an enhanced reflection rather than absorption. The basic rate equation from Eq. 9 has been solved and the corresponding fluence which leads to damage (i.e. the fluence where the plasma density equals the critical plasma density) has been determined as a function of pulsewidth, as shown in Fig. 16. The equation solution is benchmarked to published data from [26], as seen in the green curve. Note that the deviation from of the modeled data from the published data stems from the fact that diffusion effects which dominate at longer pulse durations are not accounted for.

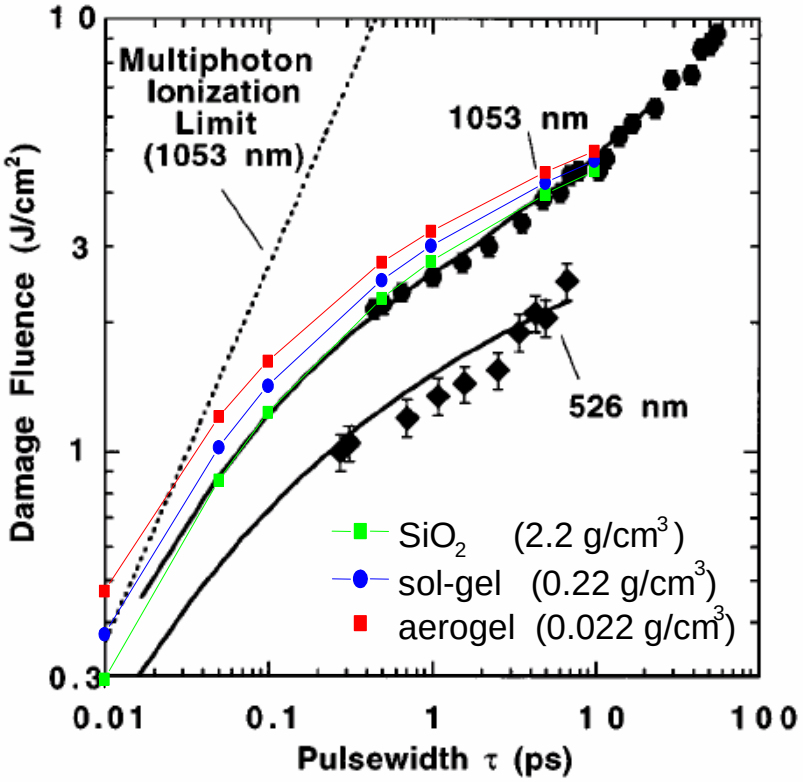

Figure 16. Comparison of damage threshold versus pulsewidth for different density materials. The modeling (in color) was benchmarked to the experimental data from [26] (in black).

To compare, the initial density conditions were reduced by one or two orders of magnitude, which is the difference in density when going from bulk fused silica density to a sol-gel or the difference in density when going from bulk fused silica density to an aero-gel respectively. The resulting curves, shown in blue (for sol-gels) and red (for aero-gels) in Fig. 16, point to a 10-20% improvement in the damage fluence compared with bulk fused silica. The key here is that sol-gels have a lower initial density, which will not affect the long pulse regime

significantly but will affect the short pulse regime. As such, sol-gels will require more intensity to reach the seed threshold for cascade ionization to take over, which in turn should slightly elevate the short-pulse damage threshold for sol-gels compared to a denser bulk fused silica.

While the modeling points to improved damage thresholds for lower density materials from the standpoint of plasma generation, the model does not account for changes in the structural integrity which may occur with such materials. Gelatin materials such as sol-gels and aero-gels are notoriously soft and are subject to easy deformation from external applied pressure. Such properties make gelatins potentially susceptible to pressure gradients which can be created with laser light and/or plasmas. Actual damage testing is required to verify the hypothesis.

4.2 Damage Testing

In order to measure the damage threshold of the various substrates the damage testing setup depicted in Fig. 17 was built.

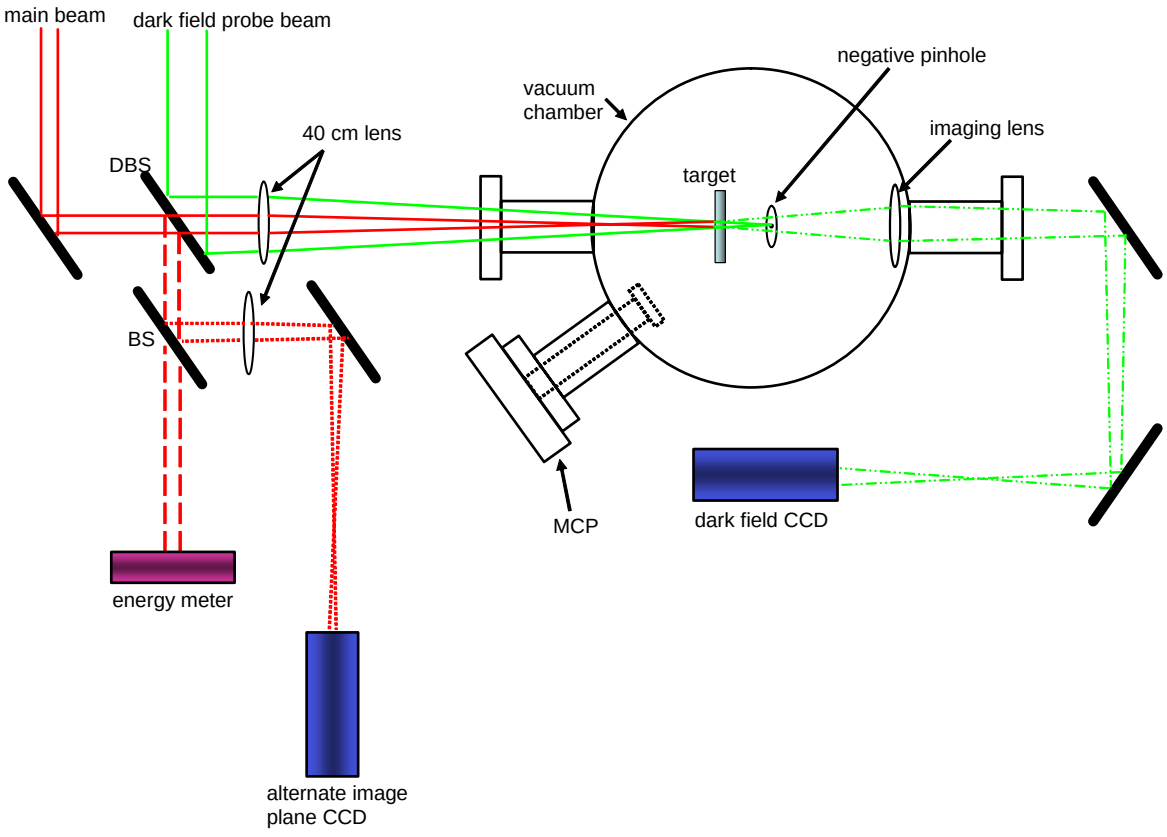

Figure 17. Overview of the damage testing setup.

The damage sample is placed into a vacuum chamber at a pressure of less than 5×10^{-6} Torr. This eliminates ionization in air and the resulting absorption and de-focusing which occurs while the beam is going through a focus as it is relay imaged onto the front surface of the target. Beam size is verified by placing a CCD camera into an alternate image plane using a second 40 cm focal length lens (see Fig. 17). The image at the target plane and the alternate image plane are compared prior to damage testing to ensure proper correlation between them. The laser beam energy is measured with a Molectron J3-05 energy meter and calibrated to the main beam. The intensity or fluence where damage occurs can be quantified via energy, target area, and pulsewidth diagnostics. Those pulsewidth diagnostics were performed using a single shot autocorrelator.

We have used two methods to quantify the onset of damage:

1. Dark-Field Scattering (DFS):

In this method a 5 mW, 532 nm continuous wave laser beam is propagated collinear to the main 1054 nm damage beam in order to illuminate the damage spot on the target surface. The green beam's divergence is adjusted in a way that its focus is about 8 cm behind the target (see Fig. 17). Using a 10 cm focal length lens, the target surface is then imaged onto a CCD camera. If the target is a transparent medium at 532 nm that shows little or no scatter, then the CCD camera will show no signal if a negative pinhole (a transparent slide with a small, circular absorber or scatterer) is placed at the focal point of the 532 nm beam. Upon damage, the sample will scatter the 532 nm beam around the obstacle in the focal plane causing light detection on the dark field CCD.

Measurements were performed by taking the background image of an unperturbed sample spot and subtracting it from the scattered light image caused by a damage spot. The onset of damage was determined by plotting the number of bright (non-zero) pixels versus laser fluence. Figure 18 shows a typical background and damage image as well as the processed data.

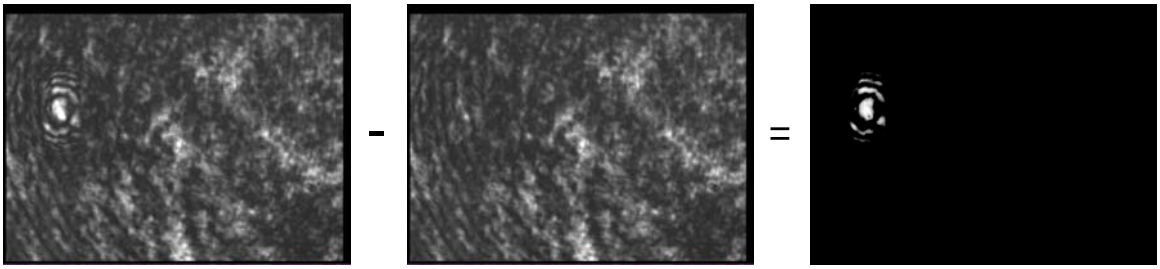

Figure 18. Typical single shot damage on a fused silica sample.

2. Ion detection via a micro-channel plate (MCP):

We have also developed an entirely new method for measuring the onset of damage with high accuracy. This method uses a micro-channel plate to detect positive ions that are liberated when surface damage occurs. Figure 19 shows a schematic of the MCP assembly.

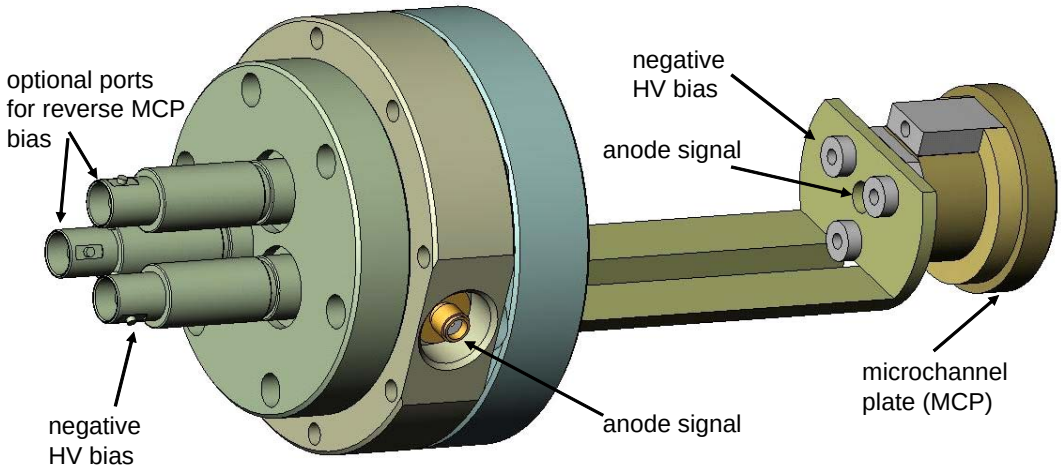

Figure 19. Schematic of the MCP assembly.

The MCP is biased to -1800 V and is placed 10 cm from the target surface. When laser damage occurs, ions are liberated from the front surface and can be detected by the MCP. The sensitivity can be varied by adjusting the MCP bias voltage from -1600 to -2200 V. The main benefit in using this method is that it doesn't require careful alignment and that its results are independent of the particular setup. The MCP can also serve as a time of flight (TOF) detector. A careful analysis of the detected voltage pulse can reveal the ion species that have been ablated from the surface. One should note that an MCP should only be operated at pressures around 10^{-6} Torr which restricts this method to vacuum damage testing. Figure 20 shows a typical voltage pulse recorded by the MCP.

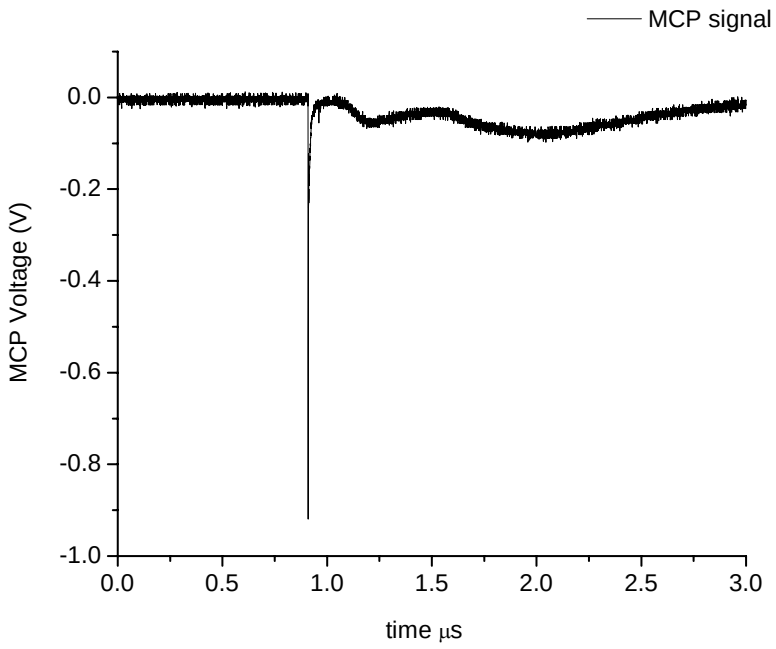

Figure 20. Voltage signal from the MCP.

Single Shot Measurements were performed as follows: Prior to every shot, a background image of the dark-field scatter CCD was recorded. An electronic signal was used to open a shutter and to trigger the alternate image CCD camera as well as the single shot autocorrelator. The MCP signals were triggered on the laser light pulse itself using a fast (10 ns rise time) photo diode. Using the light signal as a t=0 starting point will allow for TOF measurements. After each laser pulse, the MCP signal trace, the laser beam energy, the pulsewidth, the DFS image, and the beam profile in the alternate image plane were recorded. The position of every damage spot was carefully recorded and could be correlated to later measurements with a microscope. Onset of damage was determined by plotting the number of bright pixels in the DFS image as well as the MCP voltage signal versus fluence. Figure 21 shows the normalized signals for both methods versus laser fluence for a single shot damage measurement of fused silica at a pressure of less than 5×10^{-6} Torr.

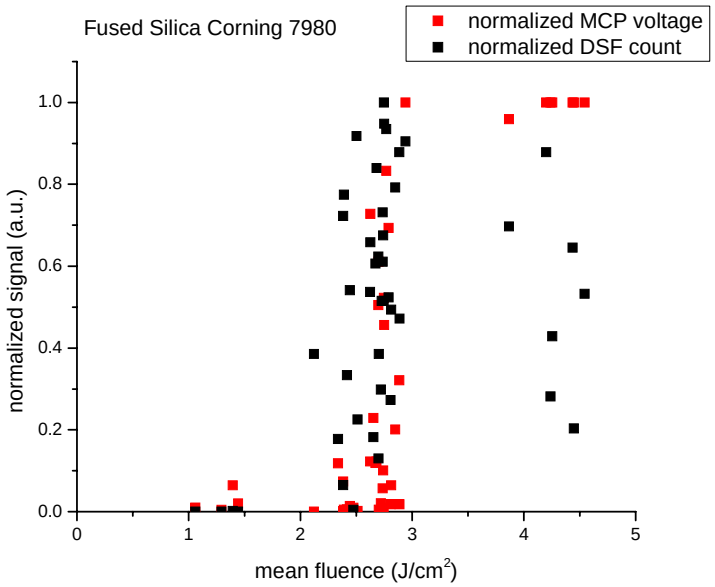

Figure 21. Plot of normalized DFS and MCP voltage versus fluence.

One can see an excellent correspondence between the DFS signals and the MCP data. The data shows a steep rise in signal strength at around 2.4 J/cm^2 with statistical fluctuations up to 3.0 J/cm^2. This threshold value corresponds very well with measurements that have been performed by Perry et. al [31]. The result verifies the suitability of an MCP for detecting the onset of damage.

Extensive damage studies on several materials have been performed using the above outlined methods. The 1053 nm laser beam energy was varied while the pulsewidth was kept at around 800 fs and the illuminated target area was 150 μm in diameter. Single shot damage threshold was determined by recording the fluence at the first sign of damage, meaning either the onset of scattering in the DFS setup or the occurrence of a voltage pulse in the MCP. Table 4 shows the obtained results for the dark field scattering technique as well as the MCP voltage measurements. For comparison, Table 5 shows the available published laser damage threshold values for fused silica. The main results are that silica aerogels exhibit a lower damage threshold than bulk fused silica, which implies that the modeled behavior is inaccurate, possibly due to the previously mentioned lack of inclusion of pressure effects in the model. However, the damage threshold of the unpatterned aerogel still exceeds that of unpatterned gold coatings (about 0.6J/cm^2, which lowers to around 0.4J/cm^2 due to field enhancements when used in a grating), as does the value for DCG.

Table 4. Measured Laser Damage Thresholds for 1053nm at 800fs

Material	Environment (Air, Vacuum)	Damage Threshold from DFS (J/cm^2)	Damage Threshold from MCP (J/cm^2)
fused silica (Corning 7980)	Vacuum	2.40	2.34
dichromated gelatin (5μm thick, 2.5 minutes fixing)	Vacuum	1.95	1.97
Dichromated gelatin (5μm thick, 2.5 minutes fixing)	Air	2.05	N/A
sonicated aerogel (4.5μm thick, n=1.074)	Vacuum	0.65	0.65
vertishear silica aerogel (2.4μm thick, n=1.05)	Vacuum	0.96	0.95

Table 5. Fused Silica Damage Thresholds

Authors	Wavelength (nm)	Pulsewidth (ps)	Damage Fluence (J/cm^2)	Damage Environment (Air/Vacuum)	Number of Pulses
Perry *et al* [31]	1053	10	4.1	Air	600
	1053	1	2.5	Air	600
	1053	0.1	1.2	Air	600
Lenzner *et al* [32]	780	1	6.0	Air	50
	780	0.05	3.3	Air	50
Tien *et al* [33]	800	1	5.2	Air	1
	800	0.1	3.3	Air	1
Ashkenasi *et al* [34]	800	0.1	3.6	Vacuum	1
	800	0.1	1	Vacuum	100

5. Chemistry and Achievable Index Modulation

5.1 Approach

Optical patterning of average properties of disordered sol-gel films for fabrication of optical elements such as waveguides [35] and diffraction gratings [16] is well reported in the literature. These processes typically use an organosilane modified metal alkoxide, often in conjunction with a photoinitiator to locally polymerize the organosilane. We have recently shown [17] that the polymerization increases the refractive index of the exposed region relative to the unexposed region ($\Delta n \approx 0.025$). Although we investigate these photosensitive sol-gel films for large area diffraction gratings, their usefulness may be limited by

a number of factors: low refractive index difference, low film thickness (and questionable UV penetration through thicker films), and 450˚C processing may be unsuitable for large area optics.

The development of coatings for large area, large-aperture high damage-threshold sol-gel diffraction gratings focused on two areas: 1) development of oxide thin films (nominal thickness ≥ 1 micron as index modulating grating structures, and 2) investigation of patterning strategies for deposited films. Because single layer, crack-free sol-gel coatings are generally limited to < 0.5 micron/layer, strategies that involve many multiple coatings or thick film concepts (e.g. aerogel) must be considered to achieve the coating thicknesses required for gratings, as suggested by modeling studies described previously. Silica aerogel thin films, currently under development at Sandia for thin film insulators and optical display applications, exhibit > 95% porosity (refractive index ~1.05-1.11) and may be deposited routinely at thicknesses exceeding one micron per layer. Aerogel films are appropriate to consider as the low-index component of a volume phase grating and may be multiply-coated for designs requiring thicknesses of several microns. The interconnected high porosity of the silica aerogel reduces the refractive index of the silica structure from 1.46 to <1.1; further, the porosity may be exploited for infiltration with a higher refractive index sol-gel material (e.g. ZrO_2, TiO_2, HfO) to achieve the required difference in refractive index between the low and high index regions of the grating. Deposition of the high refractive index phase into selected areas of the low index material may be accomplished either by selective dewetting of hydrophobic/hydrophilic regions of the aerogel film or by incorporation of a photosensitive molecule (e.g. photoacid generator) to yield denser regions (higher n) upon exposure to UV.

5.2 Background: Aerogel films

During conventional deposition of sol-gel films by dip-coating, an entrained inorganic sol is concentrated on a substrate surface by evaporation leading to aggregation and the formation of a physical or chemical gel. Continued evaporation creates liquid-vapor menisci, which, for wetting fluids, causes the liquid to be in tension. This tensile stress in the liquid causes shrinkage (pore collapse) accompanied by continued polymerization of the gel network, resulting in irreversible drying shrinkage. The dried film remains in its most compacted state as adjacent SiOH groups react to form Si-O-Si bonds and to “lock-in” the shrunken structure. Under these conditions, the film porosity is limited to approximately 10-60%. Drying the film under supercritical conditions eliminates the liquid-vapor interfaces and the associated tension-induced shrinkage but it is not suitable for applications where retention of the high porosity of the wet gel state is desired or for film processing using continuous coating operations.

We previously developed an alternative means of preserving the porous network of the wet gel (Fig. 22, [36]) where the drying shrinkage is reversible. In this benchmark process, the hydroxylated surface of the gel is derivatized with

organosilanes via standard silylation routes [37] to form an organosilyl-terminated surface. This surface does not participate in chemical reactions (condensation, hydrogen bonding) that occur during drying and which form Si-O-Si bonds. Shrinkage of the network still occurs due to recession of the liquid-vapor menisci into the gel interior, but because the structure is not "locked-in", the elastic network progressively "springs-back" to its original highly porous state. We exploit this process to form films that retain the high interconnected porosity of the gel state (>95%) that may subsequently be selectively infiltrated with a second phase to form a patterned composite film.

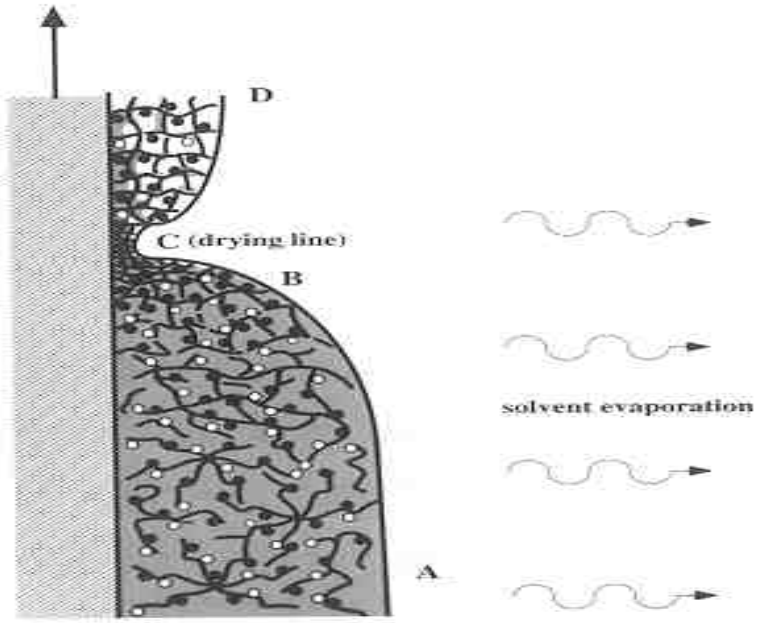

Figure 22. Schematic diagram of "springback" aerogel dip-coating process. Region A-B is pre-gelation stage. B is the gel point. Region B-C is the initial drying stage. C is the drying line. Region C-D is the final drying stage . HMDS sols exhibit expansion or springback in this region because chemical cross-linking in the fully compacted state at C is prevented by organosilyl groups allowing drying shrinkage to be reversible.

5.3 Experimental Methods

We prepared organosilyl derivatized silica sols from tetraethoxysilane (TEOS) and hexamethyldisilazane (HMDS) according to the following procedure: TEOS diluted in ethanol was partially hydrolyzed with water under acidic conditions at 60°C (molar ratios TEOS:ethanol:water:HCl = 1:3.8:1.1:$7x10^{-4}$). After 90 minutes of stirring, aqueous ammonium hydroxide was added with ethanol at room temperature resulting in final molar ratios TEOS:ethanol:water:HCl:NH_4OH = 1:38.8:3.6: $7x10^{-4}$: $2x10^{-3}$. Following gelation, the gel was aged at 50°C to strengthen the gel network, washed twice in an excess volume of ethanol, washed twice in an excess volume of hexane, and derivatized using a 5% solution of HMDS in hexane. The HMDS treated gel was again washed twice with an excess volume of ethanol to remove residual HMDS. The washed gel

was further processed to break up gel aggregates to create a fluid sol suitable for dip-coating. Post-silylation treatment included dilution with ethanol followed by sonication for 30 minutes at a power of ~95 W or mechanical shearing (Vertishear™ apparatus). Residual gel aggregates were removed by filtration prior to film deposition. The aerogel sol was stored at -20°C when not in use.

Titania sols, for use as the high refractive index phase of the grating, were first prepared using titanium tetraethoxide as the TiO_2 precursor. Because the precursor hydrolyzes so rapidly, water cannot be added directly to the alkoxide without complete hydrolysis which leads to catastrophic $Ti(OH)_4$ precipitation. Thus, titanium ethoxide was added to a 10X volume of ethanol containing 1 vol % nitric acid (70%). Water was added to the mixture to achieve a molar ratio of $H_2O/Ti(OC_2H_5)_4$ of 1:1. After addition of water, the solution pH is ~2; hydrolysis proceeds slowly without precipitation at such a low OH concentration.

A second synthesis procedure was ultimately used not only for titania but also other candidate high refractive index materials -- zirconia and hafnia. Films prepared using this process resulted in sols with a polymeric structure rather than the particulate sols prepared using the acidified alcohol procedure and, further, allowed controlled synthesis conditions by slowing the reaction rate of the precursor. Ethanol and Brij-56 surfactant were mixed and then sonicated to dissolve Brij-56. The metal chloride was added and again sonicated. Finally, propylene oxide was added (molar ratio ethanol:metal chloride:propylene oxide, 22:1:2) and the solution was aged for two hours before it was filtered. The ratio of Brij-56 to metal chloride ranged from 0 to 0.06 grams/millimole. Addition of surfactant (Brij-56) was used to induce porosity in the resulting film by serving as a templating agent [38], thus giving even more control over the possible refractive index range. In contrast, in the standard sol-gel approach to the formation of metal oxide sols, highly acidic sols are utilized to suppress the rate of condensation to minimize precipitation and facilitate the formation of homogeneous monolithic or thin-film materials. Control over sol nanostructure in this type of synthesis is often difficult, however, and conditions utilized for one type of metal oxide are generally not transferable to other elements. Our generalized strategy for producing metal oxide sols for thin film deposition utilizes a proton scavenger (propylene oxide) to control the degree of condensation in the solution, thus resulting in improved control over material nanostructure. This procedure, based on previously published routes to metal oxide xero- and aerogel materials (for example, [39]), is applicable to a wide range of materials and results in high-quality coatings on a variety of substrates.

Films were deposited by dip-coating onto silicon wafers or quartz lenses at rates ranging from 10-18 inches/min. Aerogel films were stabilized by heating for 15 minutes at 250-400°C in air; titania, zirconia and hafnia films were fired in air at 350°C for 6 hrs. Film thickness and refractive index values were determined on Si using ellipsometry at 632.8 nm wavelength.

5.4 Films for index modulating grating structures

Porous Aerogel Matrix We first demonstrated that silica aerogel films with refractive indices as low as 1.05 can be deposited as uniform films without cracking at single layer thicknesses of 0.7-1.5 micron and that thicknesses of several microns can be easily achieved over a 4" diameter sample area (see Fig. 23).

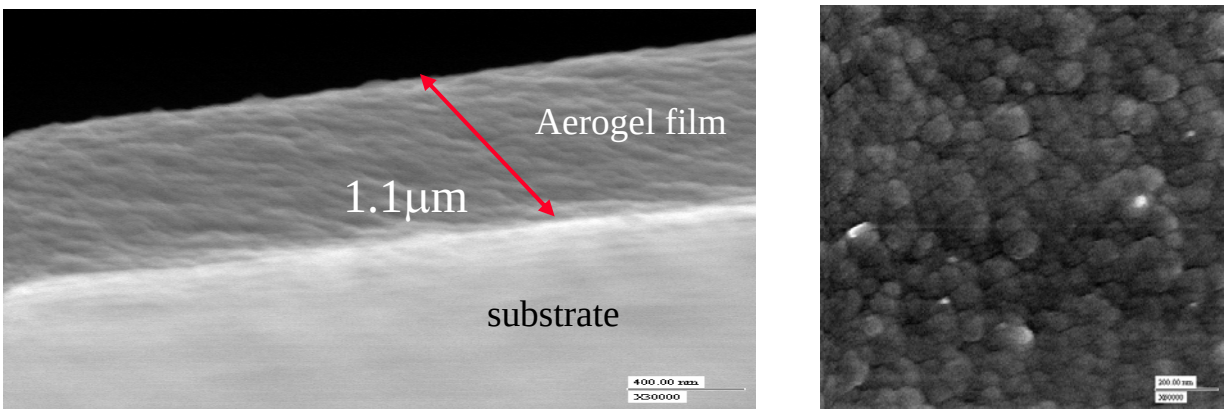

Figure 23. (Left) Cross section SEM micrograph of silica aerogel on silicon. (Right) Aerogel top view showing 10-100 nm particles.

Following silylation, we used two processes to modify the structure of the aerogel film in an attempt to further tune aerogel properties. Aggregate breakup using ultrasonic energy was compared to mechanical shearing of the aerogel structure. SEM micrographs of films deposited from these processes are shown in Fig. 24 showing clusters of aerogel particles (both images following 250°C treatment in air for 10 min) following mechanical shearing and a sponge-like structure following high-energy ultrasonic treatment. Both films exhibit ultralow refractive index, with the mechanically sheared film exhibiting a slightly lower refractive index (1.043 vs. 1.066) than the ultrasonically processed film. Film thickness was 1.06 micron and 0.81 micron for mechanical vs. ultrasonic processing, respectively. Other properties of interest in addition to optical properties include mechanical strength, light scattering, and laser damage resistance.

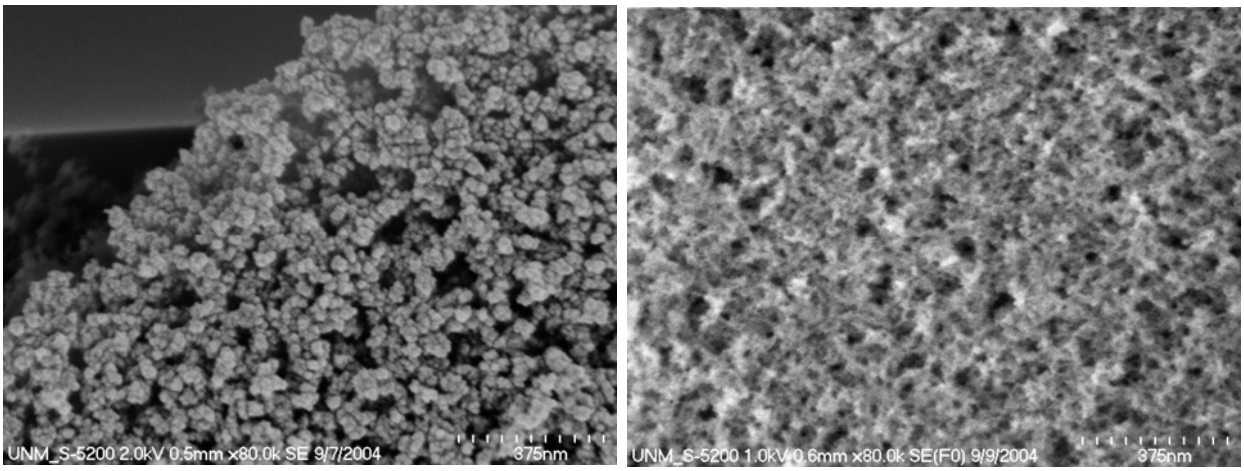

Figure 24. (Left) Mechanically sheared aerogel film. (Right) Ultrasonically processes aerogel film

Photosensitive sol-gel films To determine if photosensitive sol-gel films could be used in high-low refractive index gratings designs, we infiltrated the aerogel film matrix with silica/surfactant/photoacid generator (PAG, [diaryl iodonium hexafluoroantimonate]) [17]. In this system, silica/UV exposure through a mask at 240-260 nm causes photolysis of the PAG, releasing a strong Brønsted acid that condenses the silica matrix (and yields higher n) in the unmasked regions. The silica/surfactant/PAG system showed photoactivity upon UV exposure when the PAG was infiltrated into the aerogel matrix as a silica sol containing a non-ionic surfactant (Brij-56). Presence of the PAG within the aerogel film was qualitatively confirmed by incorporation of a pH sensitive indicator dye (ethyl violet) that turned from purple to yellow in response to the pH change caused by the PAG upon UV exposure. Yet to be investigated are the penetration depth of the PAG/silica sol into the aerogel, as well as the efficiency of UV activation (UV wavelength/intensity, PAG concentration) in thicker PAG/silica.

High Refractive Index Coatings We investigated high/low index modulation materials using sol-gel coatings, focusing on ultra-low index silica aerogel films as the low index component (thickness 1-10 microns, refractive index 1.05-1.11) and various high index refractive oxides (titania, zirconia, hafnia, refractive index ranging from 1.6-2.2) as infiltrants into the porosity of the aerogel. We studied infiltration of aerogel porosity using ZrO_2 (propylene oxide process) and TiO_2 (nitric acid process). Figure 25 shows films infiltrated with TiO_2 ($n \approx 2.2$) with $\Delta n = (n^{composite} - n^{aerogel}) = 0.14$. The similarity in refractive index between aerogel and the aerogel/ TiO_2 composite suggests that titania infiltration may be limited to the near surface region or may be sporadically deposited on the aerogel surface. The nitric acid titania synthesis procedure was replaced by the propylene oxide procedure to enhance full penetration into the matrix and similar propylene oxide synthetic routes were successful in producing hafnia coatings (n = 1.6-1.8) which are reported in the literature to exhibit high laser damage resistance.

In marked contrast, ellipsometry (see Fig. 26) of zirconia, zirconia/silica composites, and silica aerogel alone suggest that ZrO_2 fully coats the interconnected porosity of the aerogel film, as evidenced by the refractive index similarity between zirconia and the composite. The composite refractive index is quite similar to that of zirconia, $\Delta n=(n^{composite} - n^{aerogel}) = 0.76$. The SEM/EDAX map of the zirconia infiltrated aerogel showed zirconia infiltration throughout the bulk of the aerogel.

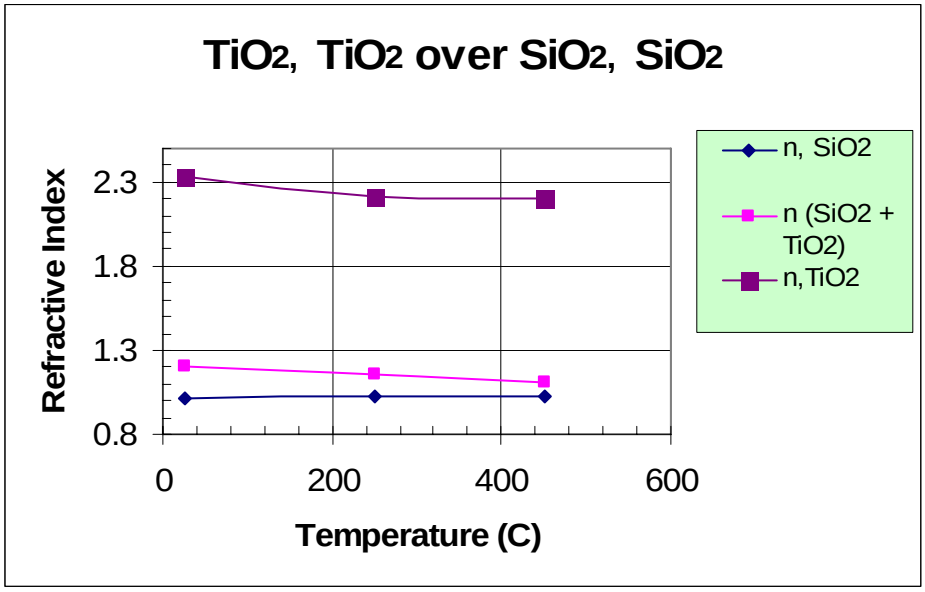

Figure 25. Refractive index (ellipsometry) of silica aerogel, aerogel/titania composite and titania as a function of temperature.

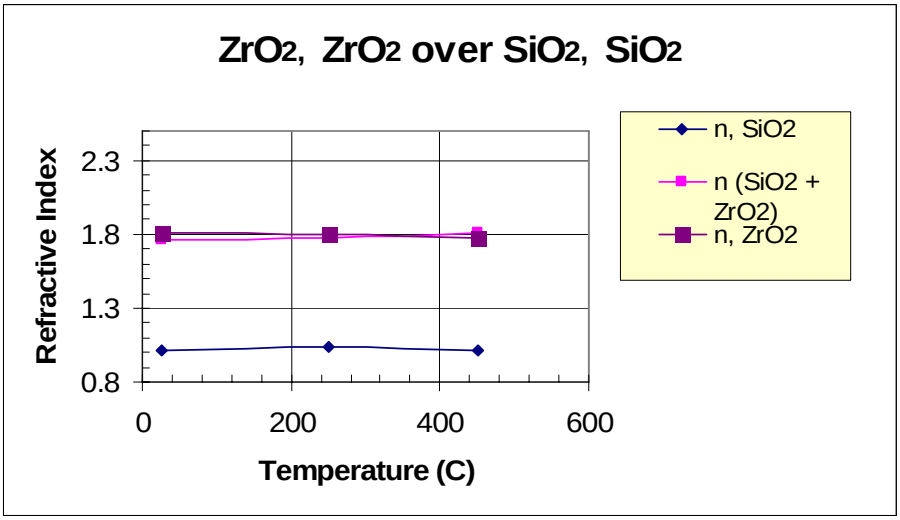

Figure 26. Refractive index (ellipsometry) of silica aerogel, aerogel/zirconia composite and titania as a function of temperature

We investigated the use of a non-ionic surfactant (Brij-56) as a structure directing (i.e. porosity forming) template to exert further "tuning" of the high refractive index phase. Table 6 shows the decrease in refractive index with increasing surfactant concentration, i.e. increase in porosity as the volume% template is increased.

Table 6: Film refractive index for chlorides of Hf, Zr, Ti as B-56/MCl_4 ratio varies

Brij-56 / MCl_4 (g/mmol)	**Film Ref. Index** M = Hf	**Film Ref. Index** M = Zr	**Film Ref. Index** M = Ti
0	1.806	1.798	1.867
0.05	1.607	1.649	1.726
0.06	1.612	1.642	1.697

Patterning of Deposited Films. Our patterning studies focused on selective dewetting as a process to pattern the aerogel film into hydrophobic or hydrophilic regions by UV/ozone treatment as a means to direct subsequent high-index film deposition to specified regions. A schematic of this process is shown in Fig. 27 where alcohol evaporation causes silica/surfactant/water enrichment in the film being deposited. The film selectively dewets the hydrophobic portion of the methyl-terminated aerogel surface so film deposition occurs only on the hydrophilic regions. This strategy can be employed with any hydrophilic sol.

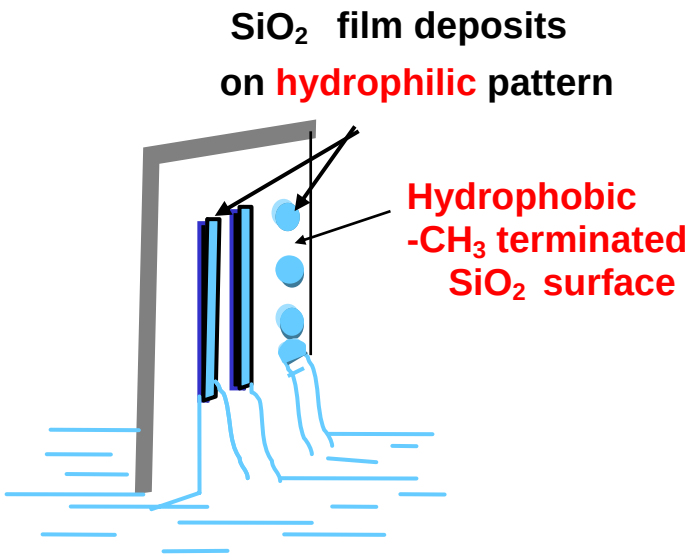

Figure 27. Schematic of selective dewetting process to deposit a high-index pattern on aerogel film.

Further control of selective dewetting can be obtained by tailoring the hydrophobicity of the surfaces. We demonstrated that the contact angle of water

on aerogel could be reversibly varied from 160° to 15° by varying surface methylation and UV/ozone treatment as shown in Fig. 28. An uncoated mercury grid lamp can be utilized to UV/ Ozone treat aerogel coatings on Si wafers to exhibit contact angles varying from 160° to 15°. The maximum required treatment time is eight minutes. Films showing 20° contact angles after UV / Ozone treatment can then be re-treated with HMDS vapors to increase contact angles up to 150°, almost entirely regaining their water repelling tendencies. These films can be patterned to create optically defined regions, such as simple microchannels progressing to more complicated patterns and images.

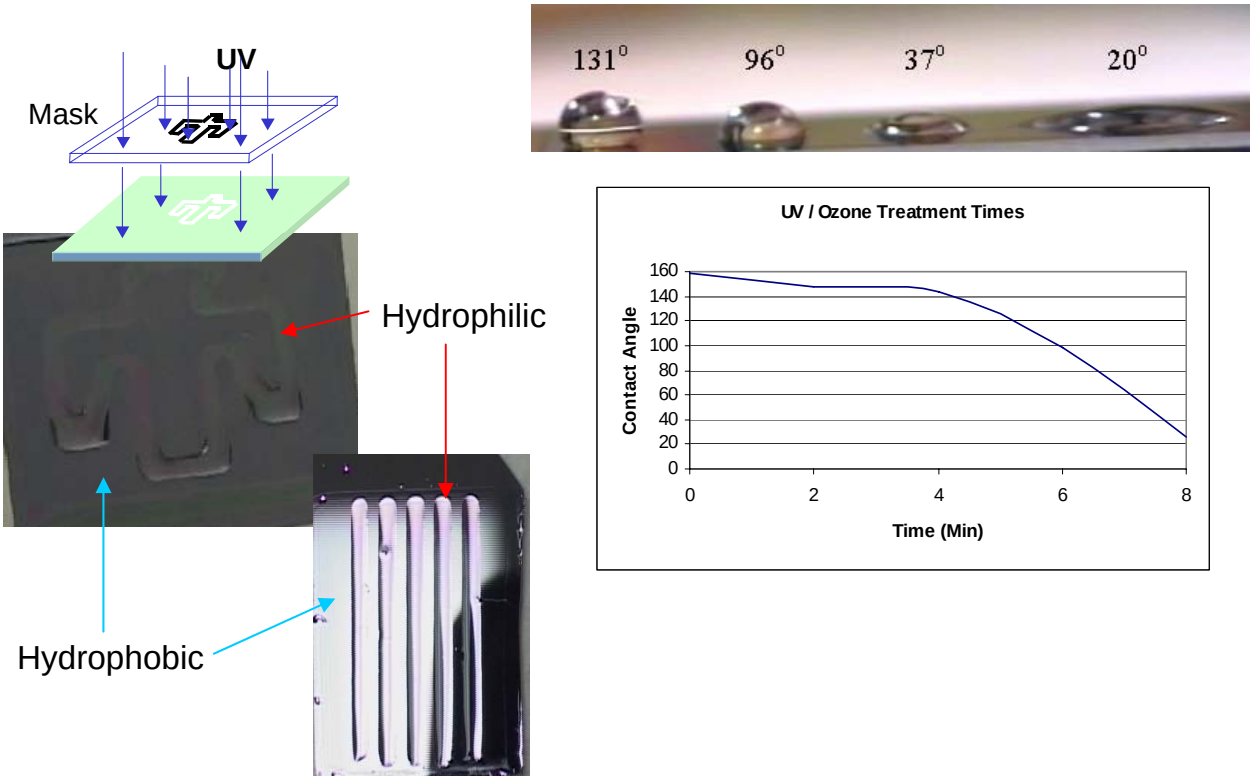

Figure 28. Hydrophobicity of film can be tailored by UV-ozone exposure

Overcoating of hydrophilic/hydrophobic patterned aerogel films with the high refractive index films (TiO_2, ZrO_2, HfO) showed poor patternability with propylene oxide derived films (due to amphiphilic nature of ethanol solvent). For comparison, we subsequently introduced a new aqueous process to prepare with alumina films (n ≈ 1.7) that showed excellent patternability (see Fig. 28 patterns). These results suggest that such patterning would allow subsequent infiltration of the high-n sols to be confined to particular regions of the film and to result in optically defined films. Modification of the propylene oxide process to increase the hydrophilic nature of the sol is needed to improve pattern selectivity of these materials. While we have shown that a substantial range of appropriate

materials options exist for formation of the low (silica, n = 1.05-1.4) and high (zirconia, titania, hafnia, alumina, n = 1.6-1.8) refractive index coatings, further investigations are needed to optimize and increase the line resolution obtainable using this technique in order to deposit precise volume phase grating structures on large area optics.

Conclusions

The idea of mirror-backed volume phase gratings for pulse compression offers several key benefits to the laser community:

- By avoiding traditional ion etching, the process could be used at a larger number of labs to custom fabricate gratings and other diffractive structures.
- The technique offers the possibility of specialized diffractive optics such as custom phase plates, Fresnel lenses, and beam samplers. Since this can be done at large-aperture, such devices could impact the traditional laser ICF community.
- By combining the thin double-pass transmission grating and mirror into a single reflection grating, one can use the strengths of normal transmission gratings without many of their weaknesses. This offers the possibility of exceedingly high damage threshold gratings (possibly >1.5 J/cm^2) in order to allow the next generation of high power lasers. At such levels, the technological pathway is facilitated towards multi-kJ-class petawatt lasers, a goal essential to Fast Ignitor fusion research at Sandia and abroad.

The prototypes developed in this research met some aspects of the criteria for a petawatt grating compressor. From section 2, these criteria were: appropriate dispersion, high diffraction efficiency, high damage threshold, large aperture capability, and vacuum compatibility. The mirror-backed DCG samples can demonstrate adequate dispersion (as measured during the diffraction efficiency tests) and fairly high diffraction efficiency. However, the issues of environmental susceptibility to water and vacuum environment incompatibility pose limitations to practical application, limitations which could possibly be overcome but only with much more work. Subsequently, the vacuum compatibility and environmental issues prevented actual grating damage studies and large aperture development. While the low damage threshold values for aerogels point to a difficulty in translating strengths of the prototype to practical use in an aerogel-based mirror-backed VPG, damage studies on the unexposed DCG material could be performed and were actually encouraging towards the fabrication of better damage threshold gratings.

References

1. D. Strickland and G. Mourou. “Compression of amplified chirped optical pulses”. **Optics Communications** v.56 n.3, (December 1, 1983), pp.219-221.

2. M.D. Perry, D. Pennington, B.C. Stuart G. Tietbohl, J.A. Britten, C. Brown, S. Herman, B. Golick, M. Kartz, J. Miller, H.T. Powell, M. Vergino, and V. Yanovsky. “Petawatt laser pulses”. **Optics Letters** v.24 n.3 (February 1, 1999), pp.160-162.

3. D.M. Pennington, C.G. Brown, T.E. Cowan, S.P. Hatchett, E. Henry, S. Herman, M. Kartz, M. Key, J. Koch, A.J. MacKinnon, M.D. Perry , T.W. Phillips, M. Roth, T.C. Sangster, M. Singh, R.A. Snavely, M. Stoyer, B.C. Stuart, and S.C. Wilks. “Petawatt laser system and Experiments”. **IEEE Journal of Selected Topics in Quantum Electronics** v.6 n.4 (July/August 2000), pp.676-688.

4. Y. Kitagawa, Y. Sentoku, S. Akamatsu, M. Mori, Y. Tohyama, R. Kodama, K.A. Tanaka, H. Fujita, H. Yoshida, S. Matsuo, T. Jitsuno, T. Kawasaki, S. Sakabe, H. Nishimura, Y. Izawa, K. Mima, and T. Yamanaka. “Progress of fast ignitor studies and Petawatt laser construction at Osaka University”. **Physics of Plasmas** v.9 n.5 (May 2002), pp.2202-2207.

5. R.D. Boyd, J.A. Britten, D.E. Decker, B.W. Shore, B.C. Stuart, M.D. Perry, and Lifeng Li. “High-efficiency metallic diffraction gratings for laser applications”. **Applied Optics** v.34 n.10 (April 1, 1995), pp.1697-1706.

6. J.A. Britten, M.D. Perry, B.W. Shore, and R.D. Boyd. “Universal grating design for pulse stretching and compensation in the 800-1100 nm range”. **Optics Letters** v.21 n.7 (April 1,1996), pp. 540-542.

7. M. Tabak, J. Hammer, M.E. Glinsky, W.L. Kruer, S.C. Wilks, J. Woodworth, E.M. Campbell, M.D. Perry, and R.J. Mason. “Ignition and high gain with ultrapowerful lasers” **Physics of Plasmas** v.1 n.5 (May 1994), pp. 1626-1634.

8. R. Kodama, et al. “Fast heating of ultrahigh-density plasma as a step towards laser fusion ignition”. **Nature** v. 412 (August 23, 2001), pp.708-802.

9. M.D. Perry, R.D. Boyd, J.A. Britten, D. Decker, B.W. Shore, C. Shannon, and E. Shults. “High-efficiency multilayer dielectric diffraction gratings”. **Optics Letters** v.20 n.8 (April 15, 1995), pp. 940-942.

10. B.W. Shore, M.D. Perry, J.A. Britten, R.D. Boyd, M.D. Feit, H.T. Nguyen, R. Chow, G.E. Loomis, and Lifeng Li. “Design of high-efficiency dielectric reflection gratings”. **Journal of the Optical Society of America A** v.14 n.5 (May 1997), pp.1124-1136.

11. M.D. Perry, D. Decker, R.D. Boyd, B.W. Shore, and J.A. Britten. “High-efficiency multilayer-dielectric diffraction gratings”. **Inertial Confinement Fusion Quarterly** v.5 n.3 (1995).

12. K. Hehl, J. Bischoff, U. Mohaupt, M. Palme, B. Schnabel, L. Wenke, R. Bodefeld, W. Theobald, E. Welsch, R. Sauerbrey, and H. Heyer. “High-efficiency dielectric reflection gratings: design, fabrication, and analysis”. **Applied Optics** v.38 n.30 (October 20, 1999), pp.6257-6271.

13. B. Wattellier, J.P. Zou, C. Sauteret, A. Migus, N. Blanchot, P.Y. Baures, D. Husson, H. Bercegol, A. Reichart, F. Bonnemason, J. Flamand, B. Touzet, and P. Neuviere. “Improved damage threshold and diffraction efficiency of gratings for ultra-bright lasers in sub-picosecond regime” **Conference on Lasers and Electro-Optics (CLEO) 2001** (CMT6), pp.98-99.

14. I.M. Thomas. “High laser damage threshold porous silica antireflective coating”. **Applied Optics** v.25 n.9 (May 1, 1986), pp.1481-1483.

15. I.M. Thomas. “Method for the preparation of porous silica antireflective coating varying in refractive index from1.22 to 1.44”. **Applied Optics** v.31 n.28 (October 1, 1992), pp.6145-6149.

16. Y. Moreau, P.Arguel, P. Courdray, P. Etienne, J.P.P. Signoret. “Direct printing of gratings on sol-gel layers”. **Optical Engineering** v.37 n.4 (April 1998), pp. 1130-1135.

17. D.A. Doshi, N.K. Huesing, M. Lu, H. Fan, Y. Lu, K. Simmons-Potter, B.G. Potter Jr., A.J. Hurd, C.J. Brinker. “Optically defined multifunctional patterning of photosensitive thin-film silica mesophases”. **Science** v.290 (October 6, 2000), pp. 107-111.

18. A.D. Razafimahatratra, M. Benatsou, M. Bouazaoui, W.X. Xie, C. Mathieu, A. Dacosta, and M. Douay. “UV-induced permanent gratings in sol-gel germanosilicate thin films”. **Optical Materials** v.13 (2000), pp.439-448.

19. H. Kogelnik. “Coupled wave theory for thick hologram gratings”. **Bell System Technical Journal** v.48 n.9 (November 1969), pp.2909-2947.

20. J.K. Rhee, T.S. Sosnowski, T.B. Norris, J.A. Arns, and W.S. Colburn. “Chirped-pulse amplification of 85-fs pulses at 250 kHz with third-order

dispersion compensation by use of holographic transmission gratings". **Optics Letters** v.19 n. 19, (October 1, 1994), pp. 1550-1552.

21. C. Horvath, A. Braun, H. Liu, T. Juhasz, and G. Mourou. "Compact directly diode-pumped femtosecond Nd:glass chirped-pulse-amplification laser system". **Optics Letters** v.22 n. 23, (December 1, 1997), pp. 1790-1792

22. B. Loiseaux, A. Delboulbe, J.P. Huignard, and F. Estable. "Phase volume holographic grating for high energy lasers". **Proceedings of the SPIE v. 3047: Second Annual International Conference on Solid State Lasers for Application to Inertial Confinement Fusion** (1996), pp.957-962.

23. D. Sheat, C. Baldwin, K. Blyth, and G. Sargood. "Mirror backed gratings for polarization independent WDM components". IEE Colloquium on Polarisation Effects in Optical Switching and Routing Systems (1990), pp. 3/1-3/2.

24. D.E. Sheat, G.R. Chamberlin, and D.J. McCartney. "Double dispersion from dichromated gelatin volume transmission gratings". **Proceedings of the SPIE v. 1461: Practical Holography V** (1991), pp.35-38.

25. D.E. Sheat and A.J.M. Miles. "Volume transmission gratings in dichromated gelatin for near infrared applications". **International Conference on Holographic Systems, Components, and Applications** (1991), pp.83-87.

26. B.C. Stuart, M.D. Feit, S. Herman, A.M. Rubenchik, B.W. Shore, and M.D. Perry. "Optical Ablation by high-power short-pulse lasers". **Journal of the Optical Society of America B** v.13 n.2 (February 1996), pp.459-468.

27. P. Prene, J.J. Priotton, L. Beaurain, and P.Belleville. "Preparation of a sol-gel broadband antireflective and scratch-resistant coating for amplifier blastshields of the French laser LIL". **Journal of Sol-Gel Science and Technology** v.19 (2000), pp. 533-537.

28. GSolver v4.20b software, Grating Solver Development Company (D. Fluckiger, P.O.Box353, Allen TX 75002), 2002.

29. Ralcon website. http://www.xmission.com/~ralcon/phasemat.html, 2003.

30. N. Chateau, J.C. Saget, and P. Chavel. "Diffraction Analysis and Experimental Investigation of Reflection-Free Holographic Phase Gratings". **Pure Applied Optics** v.2 (1993), pp.299-314.

31. M.D. Perry, B.C. Stuart, P.S. Banks, M.D. Feit, V. Yanovsky, and A.M. Rubenchik. "Ultrashort-pulse laser machining of dielectic materials". **Journal of Applied Physics** v.85 n. 9, (May 1, 1999), pp.6803-6810.

32. M. Lenzner, J. Kruger, S. Sartania, Z. Cheng, Ch. Spielmann, G. Mourou, W. Kautek, and F. Krausz. “Femtosecond Optical Breakdown in Dielectrics”. **Physical Review Letters** v. 80 n. 18 (May 4, 1998), pp. 4076-4079.

33. A-C Tien, S. Backus, H. Kapteyn, M. Murnane, and G. Mourou. “Short-Pulse Laser Damage in Transparent materials as a Function of Pulse Duration”. **Physical Review Letters** v.82 n.19 (May 10, 1999), pp.3883-3886.

34. D. Ashkenasi, M. Lorenz, R. Stoian, and A. Rosenfeld. “Surface Damage Threshold and Structuring of Dielectrics Using Femtosecond Laser Pulses: The Role of Incubation”. **Applied Surface Science** v. 150 (1999), pp.101-106.

35. A. Selvarajan and T. Srinivas. “Optical amplification and photosensitivity in sol-gel based waveguides”. **IEEE Journal of Quantum Electronics** v. 37 n.9 (2001), pp. 1117-1126.

36. S.S. Prakash, C.J. Brinker, A.J. Hurd and S.M Rao. “Silica aerogel films prepared at ambient pressure by using surface derivatization to induce reversible drying shrinkage”. **Nature** v.304, (March 30,1995), pp. 439-443.

37. E.P. Plueddemann, **Silane Coupling Agents** (Plenum, New York, 1991).

38. H. Fan, S.T. Reed, T. Baer, R. Schunk, G.P. Lopez, and C.J. Brinker. “Hierarchically structured functional porous silica and composite produced by evaporation induced self-assembly”. **Microporous and Mesoporous Materials**, vol. 44-45 (2001), pp.625-637.

39. A.E. Gash, T.M. Tillotson, J.H. Satcher Jr., L.W. Hrubesh, and R.L. Simpson. “New sol-gel synthetic route to transition and main-group metal oxide aerogels using inorganic salt precursors”. **Journal of Non-Crystalline solids**, vol. 285 (2001), pp.22-28.

DISTRIBUTION:

1	MS	0959	Scott T. Reed, 14154
1		1152	William A. Johnson, 1642
1		1193	Patrick K. Rambo, 1673
1		1193	Jens Schwarz, 1673
1		1193	Ian C. Smith, 1673
1		1349	Carol S. Ashley, 18431
1		1349	Eric D. Branson, 18431
1		1349	Adam W. Cook, 18431
1		1349	Darren R. Dunphy, 18431
1		0123	Donna L. Chavez, 1011
1		9018	Central Technical File, 8945-1
2		0899	Technical Library, 9616